PHYSICAL REVIEW B **88**, 134207 (2013)

Coarse-grained kinetic Monte Carlo simulation of diffusion in alloys

Thomas Garnier[1,2,*] and Maylise Nastar[1]
[1]*CEA, DEN, Service de Recherches de Métallurgie Physique, F-91191 Gif-sur-Yvette, France*
[2]*Department of Materials Science and Engineering, University of Illinois, Urbana-Champaign, Illinois, USA*
(Received 3 September 2013; revised manuscript received 15 October 2013; published 31 October 2013)

We present a coarse-grained Monte Carlo method designed for the simulation of vacancy-mediated diffusion phenomena. A coarse-grained master equation is derived from the atomic scale master equation using an assumption of local equilibrium within each coarse-grained cell. Atomic kinetic Monte Carlo (AKMC) simulations are used to perform both the thermodynamic and the kinetic parametrization of the coarse-grained simulations. Quantitative reproduction of flux couplings is achieved in the coarse-grained simulation. The ability of the CKMC method to simulate kinetics controlled by diffusion such as a precipitate dissolution and the decay of sinusoidal modulations of the concentration field is illustrated on body-centered-cubic (bcc) model alloys with a clustering tendency. It is shown on the case of a model of the Fe-Cu alloy previously developed that the use of this method can reduce the computational cost of a kinetic simulation by several orders of magnitude.

DOI: 10.1103/PhysRevB.88.134207 PACS number(s): 66.30.Lw, 61.43.Bn, 61.80.−x

I. INTRODUCTION

The microstructure of alloys determines to a large extent their physical and mechanical properties. It has been shown that in crystalline alloys, atomic diffusion controls the chemical homogenization of castings[1,2] and the rate of precipitation of second phases during heat treatments.[3,4] The predominant mechanism of diffusion in alloys is the vacancy mechanism. Exchanges of vacancies with neighboring atoms lead to atomic fluxes. The mediation of the exchanges by the dilute vacancies and the differences between exchange frequencies induce deviations of the atom and vacancy migration paths from a random path. These kinetic correlations lead to couplings between atomic fluxes. Strong kinetic correlation effects are known to induce phenomena such as the dragging of solute atoms by vacancies.[5] A spectacular example of flux coupling is the radiation induced segregation (RIS): under irradiation, point defects that are created in the bulk tend to migrate toward point defect sinks like dislocations or grain boundaries. The kinetic coupling between point defects and atoms produces atomic fluxes which can lead to heterogeneities of the concentration field, as observed, for example, in austenitic steels where chromium depletion appears at grain boundary under irradiation.[6–8]

The evolution of these microstructures can be quantitatively predicted using atomic kinetic Monte Carlo (AKMC) simulations based on a vacancy diffusion mechanism.[2,4,9] While they provide impressive results on the early stages of a two-phase separation and ordering kinetics, they are rapidly limited by the cost of CPU time and fail to predict late stage kinetics. A multiscale approach for dilute systems, coupling density functional theory calculations, atomic kinetic Monte Carlo models, and mesoscale methods such as cluster dynamics[10] and event-based Monte Carlo[11] bridges the gap between atomic scale diffusion mechanisms and long-term microstructure evolutions. This kind of approach remains, however, to be done for concentrated alloys.

RIS can be qualitatively simulated using continuous diffusion models.[12] These simulations rely on the out of equilibrium thermodynamic equations that relate the flux J_α through a surface S of an atomic species α to a linear combination of the gradient of chemical potential μ^β of all the atomic species β through the Onsager matrix $L_{\alpha\beta}$:

$$J_\alpha = -S \sum_\beta L_{\alpha\beta} \nabla \left(\frac{\mu^\beta}{k_B T} \right), \tag{1}$$

where k_B stands for the Boltzmann constant and T for the temperature. Continuous diffusion models are, however, limited by their deterministic nature that limits their field of application. Another efficient approach for the simulation of microstructural evolutions consists in using stochastic coarse-grained methods. The phase field method[13–17] proved to be very efficient for describing elastic effects on the microstructure.[14,18] Coarse-grained Monte Carlo simulations were applied with success to chemical adsorption[19–22] and to the diffusion of charge defects.[23] A coarse-graining procedure consists in dividing a system defined at a given scale into cells defined at a larger scale. Subcell degrees of freedom are integrated to provide kinetic equations at the coarse-grained scale that describe the evolution of the system with fewer variables. Assuming that a local equilibrium is established in every cell, a coarse-grained free-energy functional of the Ginzburg-Landau type is obtained that can be used as the force driving the evolution of the system.[24,25] Following that path, a method has been proposed to produce quantitative phase field simulations of diffusional phase transformation.[26] This method provides a Ginzburg-Landau functional able to reproduce most thermodynamic properties, like phase separation. This method differs from earlier coarse-grained Monte Carlo simulations[19,21,22] both from a thermodynamic and from a kinetic point of view. From a thermodynamic point of view, the introduction of an interaction term between cells in Refs. 26 and 27 allows the simulation of phase transition, which is impossible with the energy functional used in Refs. 19,21, and 22. From a kinetic point of view, a simplified description of the diffusion mechanism by means of direct exchanges between atoms without vacancies is chosen in Ref. 26, while vacancy-mediated diffusion is used in Refs. 19,21, and 22. The choice in Ref. 26 of direct exchanges between atoms does not allow addressing the flux couplings in alloys. However, the averages performed in coarse-grained Monte Carlo simulations neglect the nondiagonal terms of the Onsager matrix.[20,21] As a consequence, both methods prevent the study of RIS. Moreover, even in the case of thermal phase transformations, AKMC simulation studies have shown the importance of introducing a detailed description of the vacancy diffusion mechanism and the kinetic couplings.[2,4,9]

Focusing on kinetic correlations and flux couplings, we propose in the present work a method to obtain coarse-grained simulations consistent both from a kinetic and from a thermodynamic point of view with the atomic-scale simulations. Using Ref. 27 for the thermodynamic aspects, the present work is dedicated to the kinetic aspects, with a focus on the reproduction of kinetic correlations. In Sec. II, the transition from atomic-scale kinetic Monte Carlo (AKMC) simulations to coarse-grained kinetic Monte Carlo simulations (CKMC) is presented. The atomic-scale master equation is coarse-grained, which allows relating the coarse-grained transition events to the Onsager matrix and to ensure a proper reproduction of kinetic correlations. In Sec. III, the consistency of CKMC simulations with AKMC simulations is first shown on three model body centered cubic (bcc) systems: an ideal solid solution, a model alloy with first nearest neighbor (n.n.) interactions, and a model of the Fe-Cu alloy previously developed.[9] The ability of the method to accurately reproduce the Onsager matrix, the free energy of a system and the relaxation time of a sinusoidal excitation is demonstrated. Comparisons between AKMC and CKMC simulations are then performed to demonstrate the ability of CKMC simulations to provide results in quantitative agreement with AKMC simulations and to explore the possibilities and limits of the CKMC method.

II. PRINCIPLES OF COARSE-GRAINED KINETIC MONTE CARLO SIMULATIONS

Atomic kinetic Monte Carlo (AKMC) simulations have proved their reliability and will serve as a reference throughout this work. After introducing briefly that method, the master equation, on which AKMC simulations rely, is used to build a coarse-grained master equation. The kinetic parameters appearing in the coarse-grained master equation are then related to the Onsager matrix and the conditions required to describe flux couplings are defined. On that basis, the coarse-grained kinetic Monte Carlo (CKMC) method is then described.

A. From the atomic to the coarse-grained description

1. *Atomic master equation and AKMC simulations*

AKMC simulations rely upon a description of an alloy at the atomic scale. In these simulations, each vertex i of a rigid lattice corresponds to an atomic site of the crystal lattice, to which is associated an occupancy vector $\mathbf{n} = (n_i^\alpha)$, where n_i^α is either equal to 1 if the site i is occupied by the species α, or null otherwise. Let $P(\mathbf{n},t)$ be the probability to find the system in a configuration $\mathbf{n}$ at time t, the evolution of the system is controlled by the atomic-scale master equation

$$\frac{dP(\mathbf{n},t)}{dt} = \sum_{\dot{\mathbf{n}}} w(\dot{\mathbf{n}} \to \mathbf{n},dt)P(\dot{\mathbf{n}},t) - \sum_{\dot{\mathbf{n}}} w(\mathbf{n} \to \dot{\mathbf{n}},dt)P(\mathbf{n},t), \qquad (2)$$

where $w(\mathbf{n} \to \dot{\mathbf{n}},dt)$ is the probability of a system initially in the configuration $\mathbf{n}$ to be in the configuration $\dot{\mathbf{n}}$ after a time dt. In all generality, this jump probability depends on the time t of the event. However, as the time scale at which atoms jumps from site to site is much larger than the time scale of vibration of the lattice in a given configuration, atomic diffusion events can be considered as independent from the past history of the system and the evolution of the system at that scale to be a Markov process. This last property is required to simulate the evolution of the system by means of a Monte Carlo algorithm.

For that purpose, the values of the jump probabilities must be defined. Each of the local clusters of atomic sites (pairs, tetrahedra, etc.) can be associated with an atomic interaction according to their occupancies. In the following, we restrain our discussion to a binary alloy AB with vacancies. Atoms of species A and B interact with each other or with the vacancies V through pair interactions only. The energy of the system in any given configuration can thus be expressed using the following Hamiltonian:

$$\mathbb{H}(\mathbf{n}) = \frac{1}{2}\sum_{l}\sum_{(i,j)}\sum_{\{(\alpha,\beta)\in\{A,B,V\}^2\}} \gamma_{ij}^l V_l^{\alpha\beta} n_i^\alpha n_j^\beta, \qquad (3)$$

where $V_l^{\alpha\beta}$ is the interaction energy between the two species α and β at a distance l, γ_{ij}^l is the adjacency matrix, which is equal to 1 if sites i and j are lth nearest-neighbor (n.n.) sites, and where the sum over i,j is performed over each pair of sites of the system. According to the transition state theory,[28,29] the jump probability per unit time $w(\mathbf{n} \to \dot{\mathbf{n}})$ can be written as

$$w(\mathbf{n} \to \dot{\mathbf{n}}) = \nu^0_{\mathbf{n}\to\dot{\mathbf{n}}} \exp\left[-(k_B T)^{-1}\left(E^s_{\mathbf{n}\to\dot{\mathbf{n}}} - \mathbb{H}(\mathbf{n})\right)\right], \qquad (4)$$

where $\nu^0_{\mathbf{n}\to\dot{\mathbf{n}}}$ is the attempt frequency, $E^s_{\mathbf{n}\to\dot{\mathbf{n}}}$ is the energy of the system in the saddle point position between the two configurations, and $\mathbb{H}(\mathbf{n})$ is the energy of the system in the initial configuration. In a vacancy-mediated diffusion mechanism, to which we restrain ourselves in the present work, the list of configurations at reach at each step corresponds to all the configurations obtained by exchanging the position of a vacancy with one of its nearest-neighbor atoms.

2. *Coarse-grained master equation*

The equation driving the evolution of the system at a larger scale can be obtained by coarse-graining the atomic-scale master equation (2). Each site n of the coarse-grained lattice is called a cell and corresponds to a group of N_{tot} atomic sites; its state is described using an occupancy vector $\mathbf{N} = (N_n^\alpha)$, where N_n^α is the number of atoms of type α in the cell n, with $\sum_\alpha N_n^\alpha = N_{\text{tot}}$. As a consequence, all spatial information within a cell is lost, and only the spatial information at the coarse-grained scale remains. The probability $P(\mathbf{N},t)$ to find the system in a given coarse-grained configuration $\mathbf{N}$ can be deduced from the atomic-scale probabilities: $P(\mathbf{N},t) = \sum_{\{\mathbf{n}/\mathbf{N}\}} P(\mathbf{n},t)$. Similarly, the atomic master equation (2) can be summed over the atomic configurations corresponding to a single coarse-grained configuration:

$$\begin{aligned}\frac{dP(\mathbf{N},t)}{dt} &= \sum_{\{\mathbf{n}/\mathbf{N}\}}\sum_{\dot{\mathbf{n}}} w(\dot{\mathbf{n}}\to\mathbf{n},dt)P(\dot{\mathbf{n}},t)\\ &\quad -\sum_{\dot{\mathbf{n}}} w(\mathbf{n}\to\dot{\mathbf{n}},dt)P(\mathbf{n},t). \end{aligned}\tag{5}$$

The terms are then reorganized using the transition rate $W(\mathbf{N}\to\dot{\mathbf{N}},t,dt)$ to go from one coarse-grained configuration to another and the conditional probability $P(\dot{\mathbf{n}}/\dot{\mathbf{N}},t)$ to find the system in a configuration $\dot{\mathbf{n}}$ at time t knowing that the whole system is in a coarse-grained configuration $\dot{\mathbf{N}}$:

$$\begin{aligned}\frac{dP(\mathbf{N},t)}{dt} &= \sum_{\dot{\mathbf{N}}}\sum_{\{\mathbf{n}/\mathbf{N}\}}\sum_{\{\dot{\mathbf{n}}/\dot{\mathbf{N}}\}} w(\dot{\mathbf{n}}\to\mathbf{n},dt)P(\dot{\mathbf{n}},t)\\ &\quad - w(\mathbf{n}\to\dot{\mathbf{n}},dt)P(\mathbf{n},t)\\ &= \sum_{\dot{\mathbf{N}}} P(\dot{\mathbf{N}},t)\Bigg(\sum_{\{\dot{\mathbf{n}}/\dot{\mathbf{N}}\}} P(\dot{\mathbf{n}}/\dot{\mathbf{N}},t)\sum_{\{\mathbf{n}/\mathbf{N}\}} w(\dot{\mathbf{n}}\to\mathbf{n},dt)\\ &\quad - P(\mathbf{N},t)\sum_{\{\mathbf{n}/\mathbf{N}\}} P(\mathbf{n}/\mathbf{N},t)\sum_{\{\dot{\mathbf{n}}/\dot{\mathbf{N}}\}} w(\mathbf{n}\to\dot{\mathbf{n}},dt)\Bigg)\\ &= \sum_{\dot{\mathbf{N}}}(P(\dot{\mathbf{N}},t)W(\dot{\mathbf{N}}\to\mathbf{N},t,dt)\\ &\quad - P(\mathbf{N},t)W(\mathbf{N}\to\dot{\mathbf{N}},t,dt)). \end{aligned}\tag{6}$$

The transition rates depend then upon the time t, due to the dependency of the conditional probability on this same variable. As a consequence, without extra approximation, the coarse-graining of the master equation leads to a loss of the Markov property. A local equilibrium approximation can be performed to retrieve this property; if no exchange takes place at the coarse-grained scale, the probability $P(\mathbf{n}/\mathbf{N},t)$ to find a microscopic configuration given a coarse-grained one will converge towards its equilibrium $P(\mathbf{n}/\mathbf{N})$ value after a time τ. If this equilibration time τ is shorter than the time increment dt of the coarse-grained master equation, the Markov property is thus restored, as the transient regime is integrated within the coarse-grained jump frequencies $W(\mathbf{N}\to\dot{\mathbf{N}},dt)$. As long as the inequality $\tau < dt$ holds, a Markovian coarse-grained master equation is thus obtained:

$$\begin{aligned}\frac{dP(\mathbf{N},t)}{dt} &= \sum_{\dot{\mathbf{N}}} W(\dot{\mathbf{N}}\to\mathbf{N},dt)P(\dot{\mathbf{N}},t)\\ &\quad -\sum_{\dot{\mathbf{N}}} W(\mathbf{N}\to\dot{\mathbf{N}},dt)P(\mathbf{N},t). \end{aligned}\tag{7}$$

Detailed balance at the coarse-grained scale is a direct consequence of the detailed balance at the atomic scale. The transitions between two configurations $\mathbf{N}$ and $\dot{\mathbf{N}}$ can thus be written without loss of generality as

$$W(\mathbf{N}\to\dot{\mathbf{N}}) = W^0_{\mathbf{N},\dot{\mathbf{N}}}e^{-\frac{\beta}{2}[\mathbb{H}^{\text{eff}}(\dot{\mathbf{N}})-\mathbb{H}^{\text{eff}}(\mathbf{N})]},\tag{8}$$

where the reduced exchange rate $W^0_{\mathbf{N},\dot{\mathbf{N}}}$ is a symmetric function of both configurations and $\mathbb{H}^{\text{eff}}$ is an effective Hamiltonian at the coarse-grained scale.

B. Coarse-grained jump frequencies

The coarse-grained transition frequencies involved in the coarse-grained master equation can be directly related to the Onsager matrix. The difference between kinetic correlations at the atomic scale and at the coarse-grained scale is first introduced. The coarse-grained transition frequencies are then related to the Onsager matrix.

1. Kinetic correlations

Vacancy-atom exchange frequencies that are involved in the atomic master equation do not depend on the previous jumps. However, they depend on the local surrounding of the exchanging pair. As the local surrounding results from the previous jump, kinetic correlations may occur. A typical example is the drag effect in dilute alloys, where large negative values of the off-diagonal coefficients of the Onsager matrix lead the solute atom to follow the vacancy flux. In AKMC simulations, kinetic correlations are correctly reproduced provided all the vacancy-atom exchanges are taken into account. Based on the displacement of the barycenter of atoms of species α with respect to the barycenter of atoms of species β, the terms of the Onsager matrix describe the flux coupling between the two species α and β. Let V be the atomic volume, τ the integration time, r_n the displacement of the atom n, the Kubo-Green equation expresses the terms $L_{\alpha\beta}$ of the Onsager matrix on the basis of the atomic-scale displacement in a system at equilibrium:

$$L_{\alpha\beta} = \frac{(\sum_{n\in\{\alpha\}}\Delta r_n)(\sum_{m\in\{\beta\}}\Delta r_m)}{6V\tau},\tag{9}$$

where the sums are performed over all atoms of a given species. Kinetic correlations are enhanced by discrepancies between the different jump frequencies.[5] Moreover, the highest jump frequency controls the time increment at each step of the Monte Carlo algorithm while the lowest frequency usually controls the time scale of the whole simulation. Thus, the greater the difference between the highest jump frequency and the lowest jump frequency, the lesser the efficiency of the AKMC simulation will be. Hence in strongly correlated systems such as the Fe-Cu alloys, long-stage kinetics will hardly be addressed by AKMC simulations.

The coarse-grained master equation can be integrated using a Monte Carlo algorithm (cf. Appendix A) and a time increment dt at each step. In Refs. 19 and 30, a time increment $dt > \tau$ is used and the local equilibrium approximation is considered between two steps. A different choice was made in Refs. 26 and 31, where only the peripheral sites of a cell participate to diffusion during a step. This case corresponds to a time step lower than the time to equilibrate any given cell. We choose in the current work an approach similar to the one used in Refs. 19 and 30 as the size of the integration step is directly related to the numerical efficiency of the method. A consequence is that the time scale allows multiple atomic displacements between each time step. These multiple displacements involve that between t and $t + dt$ more than two atoms might have moved, or exchanges between non-neighboring cells might have taken place.

A consequence of the local equilibrium approximation is that the knowledge of the environment of the vacancy at the atomic scale is lost between two steps. The kinetic correlations are thus expected to be reduced, as after a jump of the vacancy, if the vacancy jumps back, it can exchange with any atom of the original cell. Therefore we assume that there is no correlation induced by the displacement at the coarse-grained scale. Considering all the coarse-grained transitions would lead to a very poor computational efficiency of the coarse-grained simulations. Therefore the number of events is reduced in a controlled way to achieve realistic kinetics, but as kinetic correlations are assumed to be negligible at the coarse-grained scale, this truncation should not affect the Onsager matrix. All kinetic correlations have to be embedded directly in the exchange frequencies and retrieved in the Onsager matrix measured at the coarse-grained scale.

2. Coarse-grained fluxes

The coarse-grained master equation describes the evolution of the probabilities of the coarse-grained configurations. From a given coarse-grained configuration $\mathbf{N}$, the system evolves towards a configuration $\dot{\mathbf{N}}$ at the transition rate $W(\mathbf{N} \to \dot{\mathbf{N}})$. We consider the transition between $\mathbf{N}$ and $\dot{\mathbf{N}}$ resulting in an exchange of a group $\gamma(\dot{\mathbf{N}})$ of k atoms and vacancies through the interface between n and m. These atoms that move together or independently across the interface are described using the signed number n_γ^α of unit of the species α in the group of atoms γ that moves from cell m to cell n, with $n_\gamma^\alpha > 0$ when more atoms α moved from m to n than from n to m, and $n_\gamma^\alpha \leqslant 0$ otherwise. For example, if γ describes the exchange of an atom of type α in cell m with a vacancy in cell n, then $n_\alpha^\gamma = 1$ and $n_v^\gamma = -1$. The flux J_α of a species α per unit time through the interface between two cells n and m is given by

$$J_\alpha = \sum_{\dot{\mathbf{N}}}^{m\to n} n_\gamma^\alpha W_{\mathbf{N}\to\dot{\mathbf{N}}}. \tag{10}$$

Using Eq. (8) to develop the exchange frequency, we then obtain

$$J_\alpha = \sum_{\dot{\mathbf{N}}}^{m\to n} n_\gamma^\alpha W_{\mathbf{N},\dot{\mathbf{N}}}^0 e^{-\frac{\beta}{2}[\mathbb{H}^{\mathrm{eff}}(\dot{\mathbf{N}})-\mathbb{H}^{\mathrm{eff}}(\mathbf{N})]}. \tag{11}$$

In this last equation, the difference of effective Hamiltonian is the difference of energy of the system before and after the exchange of the atoms of the group γ between the cells n and m. This is the definition of the difference of chemical potential between the two cells $\mu_n^\gamma(\mathbf{N}) - \mu_m^\gamma(\mathbf{N})$ for the group γ in the configuration $\mathbf{N}$. For the sake of simplicity, this $\mathbf{N}$-dependency is not displayed in the following equations. Performing a Taylor expansion at first order in $\beta(\mu_n^\gamma - \mu_m^\gamma)$, the last equation becomes

$$\begin{aligned} J_\alpha &= \sum_{\dot{N}}^{m\to n} n_\gamma^\alpha W_{\mathbf{N},\dot{\mathbf{N}}}^0 \left(-\frac{\beta}{2}\right)(\mu_n^\gamma - \mu_m^\gamma) \\ &\quad + \sum_{\dot{N}}^{n\to m} n_\gamma^\alpha W_{\mathbf{N},\dot{\mathbf{N}}}^0 \left(-\frac{\beta}{2}\right)(\mu_m^\gamma - \mu_n^\gamma) \\ &= -\sum_{\dot{N}}^{m\to n} n_\gamma^\alpha W_{\mathbf{N},\dot{\mathbf{N}}}^0 \beta(\mu_n^\gamma - \mu_m^\gamma). \end{aligned} \tag{12}$$

If it is assumed that the chemical potential is a linear function of the number of atoms involved in the group γ (as it is the case for a system of cells of infinite size), we can write $\mu_n^\gamma = \sum_\sigma n_\gamma^\sigma \mu_n^\sigma$, where the sum is performed over all the species σ (including the vacancies). The flux equation thus becomes

$$J_\alpha = \sum_{\dot{\mathbf{N}}}^{m\to n} n_\gamma^\alpha W_{\mathbf{N},\dot{\mathbf{N}}}^0 \sum_\sigma n_\gamma^\sigma \beta(\mu_n^\sigma - \mu_m^\sigma). \tag{13}$$

Defining the distance d between two cells and the surface S that separates them, we introduce a matrix $(L_{\alpha\sigma})$ defined over the different species:[32]

$$L_{\alpha\sigma}(\mathbf{N}) = \frac{d}{S}\sum_{\dot{\mathbf{N}}}^{m\to n} n_\gamma^\alpha W_{\mathbf{N},\dot{\mathbf{N}}}^0 n_\gamma^\sigma. \tag{14}$$

The flux equation then takes the form

$$J_\alpha = -S\sum_\sigma L_{\alpha\sigma}(\mathbf{N})\nabla(\beta\mu^\sigma), \tag{15}$$

where $\nabla(\beta\mu^\sigma) = \beta\frac{\mu_m^\sigma - \mu_n^\sigma}{d}$. The $W_{\mathbf{N},\dot{\mathbf{N}}}^0$ frequencies are in general functions of the whole configuration before and after the exchange. However, we can assume that the coarse-grained jump frequencies depend only on the local concentrations $N_n, N_m, \dot{N}_n, \dot{N}_m$ of cells n and m in configurations $\mathbf{N}$ and $\dot{\mathbf{N}}$. This assumption is relevant for a system that displays neither long-range thermodynamic correlations nor long-range kinetic correlations (i.e., in practice for a noncritical and nonpercolating system). This dependency can be expressed in terms of averages and differences as follows:

$$\begin{aligned} W_{\mathbf{N},\dot{\mathbf{N}}}^0 &= W^0(N_n, N_m, \dot{N}_n, \dot{N}_m) \\ &= \tilde{W}^0\left(\frac{N_n + N_m}{2}, \frac{\dot{N}_n + \dot{N}_m}{2}, \frac{N_n - N_m}{2}, \frac{\dot{N}_n - \dot{N}_m}{2}\right). \end{aligned} \tag{16}$$

Moreover, the conservation of the atomic species involves that $\frac{N_n+N_m}{2} = \frac{\dot{N}_n+\dot{N}_m}{2}$. The sum performed in Eq. (14) over all configurations $\dot{N}$ then corresponds to a sum over all concentration gradients. Hence the quantity $L_{\alpha\sigma}(\mathbf{N})$ does not depend on the concentration gradient $\frac{\dot{N}_n-\dot{N}_m}{2}$, nor on the concentration gradient $\frac{N_n-N_m}{2}$ due to the detailed balance: $L_{\alpha\sigma}(\mathbf{N})$ only depends on the local concentration $c = \frac{N_n+N_m}{2}$. However, this is not the case for $\tilde{W}^0$. In the continuum limit, the concentration gradients can be neglected, but in the case of finite size cells these gradients have to be considered. This technical point is discussed in Appendix B.

The flux equation can then be written:

$$J_\alpha = -S\sum_\sigma \tilde{L}_{\alpha\sigma}(c)\nabla(\beta\mu^\sigma). \tag{17}$$

An identical flux equation is obtained from out of equilibrium thermodynamics[33] for infinite size cells. As the local mobility $\tilde{L}_{\alpha\sigma}(c)$ does not depend on the cell size, it can be identified to the Onsager matrix $L_{\alpha\sigma}(c)$ used in out of equilibrium thermodynamics, which describes the correlation between displacement of atoms of types α and σ in an environment of mean solute concentration c:

$$L_{\alpha\sigma}(c) = z^* \tilde{L}_{\alpha\sigma}(c), \tag{18}$$

where z^* is the number of nearest neighbor cells in a given Cartesian direction. Equation (14) establishes the relationship between the Onsager matrix and the kinetic events at the coarse-grained scale. The Onsager matrix can be obtained by performing AKMC simulations[34,35] or using analytical methods.[5,36] Using Eq. (9) to compute the Onsager matrix from AKMC simulation will thus allow parameterizing the coarse-grained transition frequencies.

3. Kinetic events

In order to make coarse-grained simulations computationally efficient, the ensemble of kinetic events has to be truncated. We choose to truncate it by defining a maximum size k for the groups of atoms being exchanged during a single Monte Carlo step. Hence the speed at which a larger group of atoms diffuses is the average of the diffusion speeds of its subelements. k can then be determined in order to reproduce the Onsager matrix while keeping the number of transition minimum.

For a binary alloy with vacancies on a rigid lattice, the Onsager matrix is a 3×3 matrix. However, due to site conservation, only three terms are actually independent. Using Eq. (14) that relates the Onsager matrix to the coarse-grained kinetic events, we determine the minimum group size k required to reproduce the Onsager matrix. For vacancy-mediated diffusion, an exchange involves at least a species on each side and any exchange has to involve a vacancy. For $k = 1$, there are only two different possible exchanges involving a vacancy,

$$V \leftrightarrow A \quad (VA), \quad V \leftrightarrow B \quad (VB). \tag{19}$$

This set provides only two degrees of freedom for the kinetic properties, associated with the frequency of both exchanges. As a consequence, it cannot reproduce the variety of behavior that can be displayed by the Onsager matrix with its three degrees of freedom. For $k = 2$, using all the exchanges involving up to two atoms in each cell and at least a vacancy, a set of events can be built that fulfill this objective:

$$\begin{aligned}
&V \leftrightarrow A \quad (VA), \quad V \leftrightarrow B \quad (VB),\\
&VA \leftrightarrow VB \quad (VAVB), \quad VB \leftrightarrow VA \quad (VBVA),\\
&VA \leftrightarrow BB \quad (VABB), \quad VB \leftrightarrow AA \quad (VBAA),\\
&VV \leftrightarrow AB \quad (VVAB), \quad VA \leftrightarrow AA \quad (VAAA),\\
&VB \leftrightarrow BB \quad (VBBB).
\end{aligned} \tag{20}$$

An event like the exchange $(VAAA)$ of a VA pair from one cell against a AA pair from another one is identical to the (VA) event due to the local equilibrium approximation, and as a consequence will not be further discussed. The $(VAVB)$ event is equivalent to a direct A-B exchange, but emphasizes the need of a vacancy in one of the involved cells as the direct exchange is impossible at the atomic scale. Detailed balance—which applies to this event as well as to any other—requires that its reduced exchange rate is equal to the one of the inverse jump $(VBVA)$.

Using Eq. (14), their probability can be related to the Onsager matrix. For example, for the $VABB$ exchange, we have $n^V_{VABB} = 1, n^A_{VABB} = 1, n^B_{VABB} = -2$, and thus a contribution to $L_{BB}(c)$ of $(-2)(-2)\tilde{W}^0_{VABB}(c)$, or to $L_{AB}(c)$ of $(-2)(1)\tilde{W}^0_{VABB}(c)$. We thus obtain

$$\begin{aligned}
L_{AA}(c) &= \frac{d}{S} z^* \big(\tilde{W}^0_{AV}(c) + \tilde{W}^0_{VABB}(c) + 4\tilde{W}^0_{BVAA}(c)\\
&\quad + \tilde{W}^0_{VVAB}(c) + 2\tilde{W}^0_{VAVB}(c)\big),\\
L_{BB}(c) &= \frac{d}{S} z^* \big(\tilde{W}^0_{BV}(c) + 4\tilde{W}^0_{AVBB}(c) + \tilde{W}^0_{BVAA}(c)\\
&\quad + \tilde{W}^0_{VVAB}(c) + 2\tilde{W}^0_{VAVB}(c)\big),\\
L_{AB}(c) &= \frac{d}{S} z^* \big(-2\tilde{W}^0_{VAVB}(c) - 2\tilde{W}^0_{AVBB}(c)\\
&\quad - 2\tilde{W}^0_{BVAA}(c) + \tilde{W}^0_{VVAB}(c)\big),\\
L_{AV}(c) &= \frac{d}{S} z^* \big(-\tilde{W}^0_{AV}(c) + \tilde{W}^0_{AVBB}(c)\\
&\quad - 2\tilde{W}^0_{BVAA}(c) - 2\tilde{W}^0_{VVAB}(c)\big),\\
L_{BV}(c) &= \frac{d}{S} z^* \big(-\tilde{W}^0_{BV}(c) - 2\tilde{W}^0_{AVBB}(c)\\
&\quad + \tilde{W}^0_{BVAA}(c) - 2\tilde{W}^0_{VVAB}(c)\big),\\
L_{VV}(c) &= \frac{d}{S} z^* \big(\tilde{W}^0_{AV}(c) + \tilde{W}^0_{BV}(c) + \tilde{W}^0_{AVBB}(c)\\
&\quad + \tilde{W}^0_{BVAA}(c) + 4\tilde{W}^0_{VVAB}(c)\big),
\end{aligned} \tag{21}$$

where the surface $S = d^2/4$ in the case of a bcc lattice. The direct exchange event $(VAVB)$ introduces a correlation in the displacement of A and B atoms. However, as the reduced exchange rate of each event is necessarily positive, this correlation is necessarily negative. The two-atom events $((VABB), (VBAA), (VVAB))$ are thus required to obtain all types of Onsager matrices: the $(VVAB)$ event allows positive A-B correlations, while the $(VABB)$ [respectively, $(VBAA)$] is required to obtain positive V-A [respectively, V-B] correlations, which are involved in the solute drag phenomenon.[5,37] Finally, the single atom exchanges (VA) and (VB) cannot be avoided, as their presence is required in some cases to ensure the positivity of the Onsager matrix: $L_{ii}L_{jj} \geqslant L_{ij}^2$. Therefore any Onsager matrix of a binary alloy can be obtained by exchanges involving one and two species. A subset of four or three exchange frequencies is actually sufficient to reproduce a specific Onsager matrix.

The Onsager matrix is unfortunately insufficient with its three free parameters to determine completely the values of all the different frequencies required at the coarse-grained scale. However, if these frequencies are required to cover all the cases of Onsager matrices, only a subset of them is necessary in any given situation. According to the sign of the different correlation terms of the Onsager matrix, a subset of three frequencies only can be chosen to describe the kinetic properties of the system. Their values are then entirely determined by the Onsager matrix terms. This phenomenological choice ensures both a maximum numeric efficiency by reducing the number of frequencies computed at each step and the reproduction of the averaged kinetic correlations as expressed by the Onsager matrix. As the ensemble of the events at the coarse-grained scale has been truncated, an accurate description of the fluctuations of the kinetic correlations should not be expected.

The discrete description of the vacancy concentration field affects the implementation of the events described. The

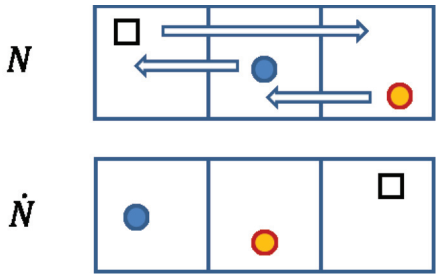

FIG. 1. (Color online) Representation of the atoms involved in a $(VVAB)$ jump, in the original configuration $\mathbf{N}$ (top) and the final configuration $\dot{\mathbf{N}}$ (bottom). The vacancy is represented by a square, while the A and B atoms are represented by a dark and a light disks.

vacancy concentration is usually very small, impairing the ability to perform the $(VVAB)$ event as the probability to find a configuration with two vacancies in a same cell vanishes. This event can be replaced by another one inducing the same kinetic correlations. For this reason, we have chosen to remove the two-vacancy event from the list and to replace it by a new event involving a single vacancy and three cells, where a single vacancy jumps twice in a given direction, while an atom A and an atom B each jumps once in the return direction. To ensure detailed balance, two cases have to be considered, in which either an atom A or an atom B jump first, as illustrated in Fig. 1.

III. CKMC SIMULATIONS

The capacity of the CKMC method to simulate diffusion in alloys has been studied on bcc alloys by performing a systematic comparison with AKMC results. The principle of the parametrization procedure is first exposed. Then, to assess the ability of the CKMC method to simulate diffusion kinetics of alloys, basic properties have been measured on three different alloys of increasing complexity: an ideal solid solution, where interatomic interactions are null, then a bcc alloy with first nearest neighbor interactions and a demixing tendency, and finally a model of the Fe-Cu alloy with first and second nearest neighbor interactions. Once the consistency of AKMC and CKMC simulations is established, the limitations and advantages of the CKMC simulations are explored.

A. Coarse-grained kinetic Monte Carlo simulation method

The coarse-grained kinetic Monte Carlo method developed in this work relies on a coarse-grained description of diffusion. Like in AKMC simulations, the alloy is described using a rigid lattice. A configuration is defined by a coarse-grained occupation vector defined over all species α and sites n at the coarse-grained scale: $\mathbf{N} = (N_n^\alpha)$. All the degrees of freedom corresponding to the position of atoms within a cell are lost. However, the occupation numbers remain discrete quantities. Thermodynamic properties of an alloy in a CKMC simulation are determined by an effective Hamiltonian at the coarse-grained scale $\mathbb{H}^{\rm eff}(\mathbf{N})$, while the kinetic properties rely on the set of reduced frequencies $\tilde{W}^0(c)$. Once all these quantities are determined, the evolution of the coarse-grained system is obtained from the coarse-grained master equation (7). A trajectory in the phase space of a given system is obtained using a Monte Carlo algorithm, e.g., the Metropolis[38] or the residence time[39] algorithms. In the present work, the latter is used in both AKMC and CKMC simulations.

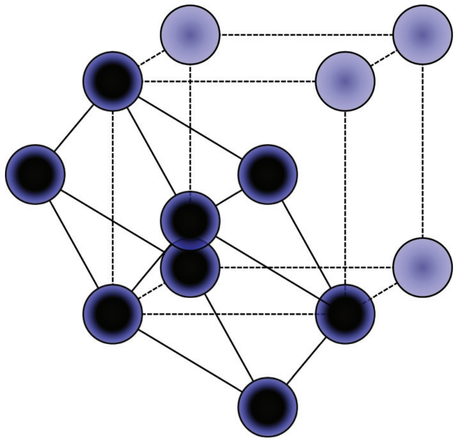

FIG. 2. (Color online) Representation of the atoms belonging to an eight atomic site cell (dark sphere) in bcc structure.

In order to numerically assess the method, a bcc lattice has been chosen where sites at the atomic scale are separated by a distance $a\sqrt{3}$. The atomic sites of a bcc structure can be grouped into cells themselves organized into a bcc lattice where each cell, containing d^3 atomic sites, is separated from its nearest neighbor by a distance $da\sqrt{(3)}$, with d taking any positive integer value. An eight-atom cell can be built by considering a cell identical to a Wigner-Seitz cell, but of twice its size in each dimension. The atomic sites forming such kind of cell are shown in Fig. 2 from which larger cells can be built by homotheticity. This allows using an identical lattice at every scale with $z^* = 4$ for a bcc lattice, without disturbing the symmetries of the crystal.

The parametrization of the effective Hamiltonian is discussed extensively in Ref. 27. It is shown that the effective Hamiltonian can take the form

$$\mathbb{H}^{\rm eff}(\mathbf{N}) = \sum_n E^d\left(N_n^B, N_n^v\right) + \frac{1}{2}\sum_l \sum_{(n,m)} \sum_{\beta\in\{B,V\}} \gamma_{ij}^l \kappa^\beta_{(\{N_n^\sigma + N_m^\sigma\})}\left(N_n^\beta - N_m^\beta\right)^2, \tag{22}$$

where the local energy E^d is the free energy of an isolated single cell and $\kappa^\beta_{(\{N_n^\sigma + N_m^\sigma\})}$ is the stiffness coefficient that controls interactions between neighboring cells.

The parametrization method proposed in Ref. 27 leads to a quantitative reproduction of the equilibrium properties of an alloy like the phase diagram, the equilibrium fluctuations of the concentration field, or the interface profile. It can be directly applied to the current cell geometry. The extension to a binary alloy including vacancies is also straightforward. It is performed by considering a local energy $E^d(N_B, N_V)$ that depends both on the solute and the vacancy concentration. This local energy term is computed in a similar way to the local energy of the binary alloy. Similarly, the local free energy is computed using the Widom scheme in a simulation box containing a single vacancy. The consideration of a ternary

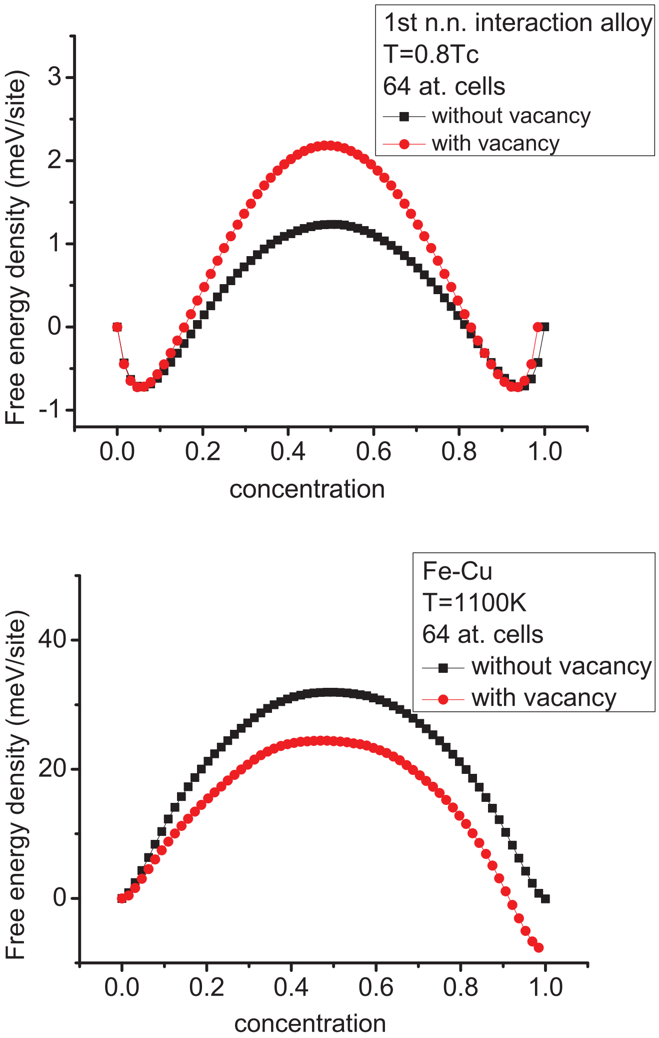

FIG. 3. (Color online) Free-energy density as a function of the concentration for the first n.n. interaction alloy at a temperature $T = 0.8T_c$ (top) and the Fe-Cu alloy at $T = 1100$ K (bottom), with and without vacancy in the system. For the sake of clarity, the reference energy is the system without B (respectively, Cu) atom. Similarly, in the Fe-Cu case, the quantity $F(c) = c \times 0.74$ eV has been subtracted from the free energy. The reference energies for the FNNI alloy with and without vacancies are, respectively, -0.108 eV and 0, and -4.64 and -4.28 eV in the case of the Fe-Cu alloy.

system increases considerably the CPU requirement of this operation. As an example, results for the local energy term of 64 atomic site systems are shown in Fig. 3 for the first nearest neighbor interacting alloy and the Fe-Cu alloy described in detail in the next section. The influence of the vacancy concentration gradient on the interaction term has, however, been neglected, allowing a parametrization procedure of the interaction term identical to the one performed in Ref. 27.

Equation (21) relates the coarse-grained average jump frequencies $\tilde{W}^0_{XY}(c)$ to the Onsager matrix and can be used for the kinetic parametrization of CKMC simulations. The Onsager matrix of an alloy is computed using Eq. (9) by applying the following procedure during an AKMC simulation: let a time τ be sufficient for the vacancy to perform 24^3 jumps, a 24^3 site system at a given concentration is equilibrated during 500τ before the Onsager matrix being measured using Eq. (9) over a time τ. The results obtained are then averaged over 50 000 iterations of the procedure.

B. Basic properties

Three different properties have first been studied on three different model alloys using both CKMC and AKMC methods to assess the consistency of the CKMC method on three model alloys of increasing complexity. For each of these alloys, the free energy is first shown to illustrate the accuracy of the thermodynamic parametrization and its ability to take into account thermodynamic finite size effects. AKMC and CKMC evaluations are performed using the Widom scheme and its coarse-grained counterpart.[27] The free energy per atomic site is represented for three different simulation boxes, a 64 atomic site system, a 4096 atomic site system composed of 4096 atomic sites within an AKMC simulation and finally a system of 4096 atomic sites divided into 64 cells of 64 atomic sites within a CKMC simulation. In order to confirm the validity of the kinetic parametrization, the Onsager matrix of each alloy is also computed using CKMC simulations for cells of $d^3 = 27$, 64, and 512 atomic sites each and compared with AKMC measurements. A procedure identical to the one described in the previous section is applied to the CKMC method to compute the Onsager matrix. The same total system size is conserved to allow an easier comparison of the results. In the following, the Onsager matrix is always represented on the figures normalized by the vacancy concentration and the lattice parameter. Finally, the decay of a sinusoidal excitation is measured to prove the ability of the method to predict out of equilibrium kinetics. These simulations involve both the driving force and the kinetic prefactor. For that purpose, in a $384 \times 48 \times 48$ site simulation box filled with a random solution, the decay of a sinusoidal excitation of the concentration field is observed. From an initial configuration of the concentration field $c = c_0 + A \sin(2\pi x/\lambda)$, where x is the position on the x axis and $\lambda = 24a$, the system evolves towards an homogeneous solution within AKMC simulations and CKMC simulations for cells of $d^3 = 27$, 64, and 512 atomic sites. The amplitude of the excitation is extracted and displayed as a function of time. In all kinetic simulations, a single vacancy is present in the simulation box.

1. Ideal solid solution on a bcc lattice

An ideal solid solution represents the simplest system in which diffusion properties can be studied. In this system, atoms do not interact with each other. As a consequence, the free energy has a purely entropic origin, and the interaction term in the effective Hamiltonian is null. The local free energy displays then a single-well profile with a minimum at a concentration $c = 1/2$, as shown in Fig. 4. A finite-size effect appears, which is perfectly taken into account by the parametrization method as can be seen by the agreement on the 4096 site system between the AKMC and the CKMC evaluation.

Given the absence of atomic interactions, the temperature does not affect the kinetic properties and correlations are small, even if some still exist due to geometrical effects induced by the lattice.[36] AKMC calculations of the Onsager matrix of this alloy are displayed in Fig. 5. The ideal solid solution presents

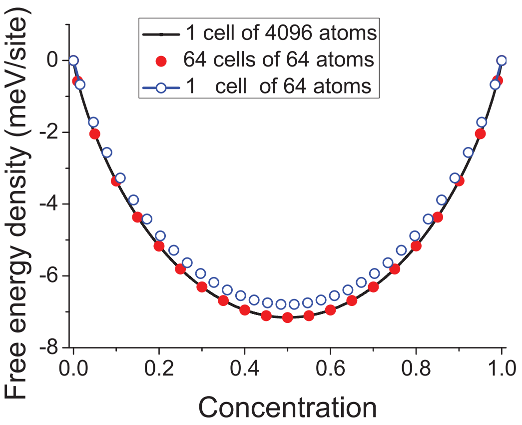

FIG. 4. (Color online) Free energy density as a function of the concentration for the ideal solid solution on a bcc lattice at $T = 550$ K. The dark line corresponds to a single AKMC system of 4096 atoms, the circles to a single AKMC system of 64 sites, the dots to a CKMC system of 64 cells of 64 atoms.

positive L_{AB} correlations at all concentration. As a consequence, only the subset $\{(AV),(BV),(VVAB),(VVBA)\}$ of coarse-grained events is necessary to describe the system at the coarse-grained scale. The average frequencies then take the values

$$\begin{aligned}\tilde{W}^0_{AV}(c) &= \frac{S}{dz^*}[L_{AA}(c) - L_{AB}(c)],\\ \tilde{W}^0_{BV}(c) &= \frac{S}{dz^*}[L_{BB}(c) - L_{AB}(c)],\\ \tilde{W}^0_{VVAB}(c) &= \frac{1}{2}\frac{S}{dz^*}[L_{AB}(c)],\\ \tilde{W}^0_{VVBA}(c) &= \frac{1}{2}\frac{S}{dz^*}[L_{AB}(c)],\end{aligned} \tag{23}$$

where $z^* = 4$ and the $\frac{1}{2}$ factor is due to the split of the (VVAB) event into two cases where either the A or the B atom jump first. A polynomial fit of the terms of the Onsager matrix computed using AKMC simulation is used to determine the CKMC jump frequencies. This parametrization leads to a perfect reproduction of the Onsager matrix by CKMC simulations as can be seen in Fig. 5, with a maximum error below 3% of the AKMC values. The agreement obtained validates in the case of the ideal solid solution the hypothesis that correlations could be neglected at the mesoscopic scale.

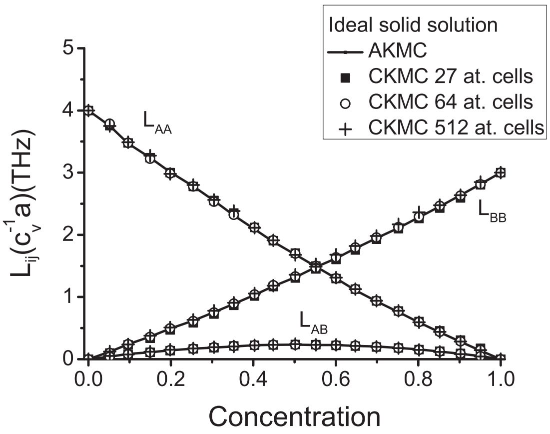

FIG. 5. Normalized Onsager matrix of an ideal solid solution on a bcc lattice as a function of the concentration. The dark line corresponds to AKMC simulations, while the symbols correspond to CKMC simulations.

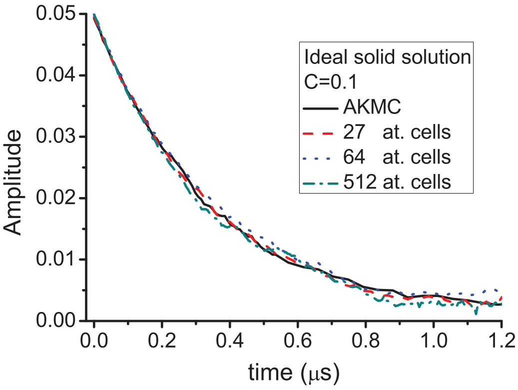

FIG. 6. (Color online) Amplitude of a sinusoidal excitation of wavelength $\lambda = 24a$ as a function of time of a solution of concentration $C = 0.1$ of an ideal solid solution on a bcc lattice. The black continuous line corresponds to AKMC simulation, while the red dashed (respectively, blue dotted and green dash and dotted) one to 27 (respectively, 64 and 512) at. cells CKMC simulations.

The simulation of the decay of a sinusoidal excitation of amplitude 5% and of wavelength $\lambda = 24a$ in a solution of concentration $c = 0.1$ in atom B is displayed on Fig. 6. It shows that in the absence of interactions, the exponential decay is recovered by CKMC simulations, and that the decay of the excitation in AKMC simulations is quantitatively reproduced by CKMC simulations for every cell size. This shows (1) that the driving force, of purely entropic origin in the present case, is correctly described and (2) that the parametrization of the Onsager matrix leads to the correct interdiffusion coefficient, as it is the kinetic quantity involved in the current simulations.

2. First nearest neighbor interaction alloy on a bcc lattice

In order to demonstrate the ability of CKMC simulations to correctly reproduce the effect of temperature, an alloy with atomic interaction is required. A binary alloy A-B with first n.n. interactions is chosen for that purpose, with a simple set of interactions leading to an unmixing tendency: only one nonzero interaction is considered, between A and B atoms $V_1^{AB} = 0.01$ eV at their equilibrium first n.n. position. No effect of the solute on the saddle point is introduced. As only pair interactions are considered, thermodynamic properties are invariant through the $c \to 1 - c$ transformation. As shown in Table I, different attempt frequencies for A and B atoms were chosen, to introduce a difference between the kinetic

TABLE I. Atomic jump attempt frequencies for the ideal solid solution (IDS) and the first nearest neighbor interaction alloy (FNNI) in terahertz.

	IDS	FNNI
$V-A$	1000	1000
$V-B$	750	750

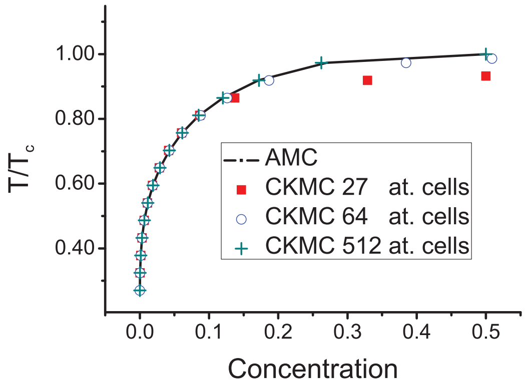

FIG. 7. (Color online) Phase diagram of the first n.n. alloy. The temperatures are normalized by the AKMC critical temperature T_c. The dark line corresponds to an AKMC system of 48^3 site system, the symbols to CKMC system with the same number of atomic sites, divided in 27 (full squares), 64 (empty circles) and 512 (plus symbols) at. cells.

properties of *A* and *B* atoms. As shown in Fig. 7, the phase diagram obtained by semi-grand-canonical simulation of a 48^3 site system displays a miscibility gap up to a critical temperature T_c where a second-order phase transition takes place. CKMC simulations accurately reproduce the solubility limit away from the direct vicinity of the critical temperature, and two specific temperatures, $T = 0.8T_c$ and $1.5T_c$, were chosen to exemplify the situation above and below the critical temperature.

As in the case of the ideal solid solution, the ability of the CKMC simulations to reproduce the free energy of an AKMC system of 4096 atomic sites is tested for this model alloy. As can be observed in Fig. 8 at $T = 1.5T_c$, a perfect reproduction of the free energy is obtained. The case of $T = 0.8T_c$ displayed in Fig. 9 shows, however, that inside the miscibility gap, a lesser accuracy is achieved, even if an excellent overall agreement is obtained. The AKMC profile appears slightly flatter in the middle of the miscibility gap. This difference might originate from the relaxation of the interfaces inside the gap. Within the miscibility gap, the system tends to separate. The finite size of the system constrains the system that might not be able to separate in this small space, while it would have given two different phases in an infinite system. The thermodynamic parametrization takes into account relaxation within the cell, but relaxation at the larger scales is only imperfectly described by the coarse-grained description.[27]

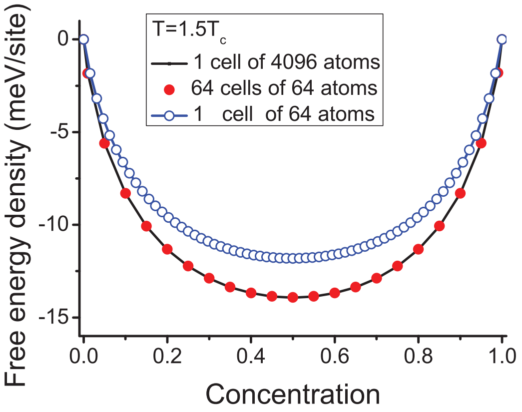

FIG. 8. (Color online) Free energy density as a function of the concentration for the first n.n. interaction alloy at a temperature $T = 1.5T_c$. The dark line corresponds to a single AKMC system of 4096 atoms, the circles to a single AKMC system of 64 sites, the dots to a CKMC system of 64 cells of 64 atoms.

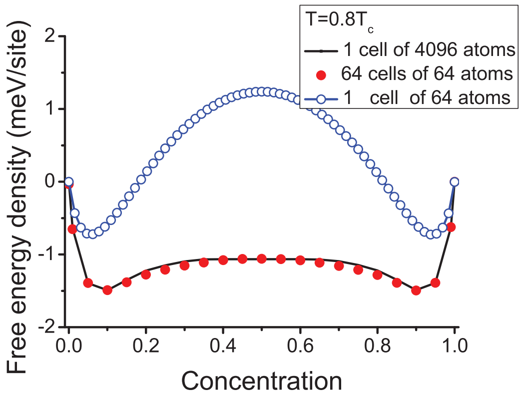

FIG. 9. (Color online) Free-energy density as a function of the concentration for the first n.n. interaction alloy at a temperature $T = 0.8T_c$. The dark line corresponds to a single AKMC system of 4096 atoms, the circles to a single AKMC of 64 sites, the dots to a CKMC system of 64 cells of 64 atoms.

The study of the Onsager matrix by AKMC simulation is performed at every concentration at $T = 1.5T_c$ and limited to concentrations below the solubility limit at $T = 0.8T_c$. The results are displayed in Figs. 10 and 11. In both cases, positive L_{AB} correlations can be noticed at every concentration. As a consequence, a set of events similar to the one used in the case of the ideal solid solution is used. Figures 10 and 11 show that CKMC simulations thus parameterized quantitatively reproduce the Onsager matrix obtained by AKMC simulations with a relative error below 3%.

Simulations of sinusoidal excitation decay were performed in the case of the first n.n. interaction alloy, as exemplified for

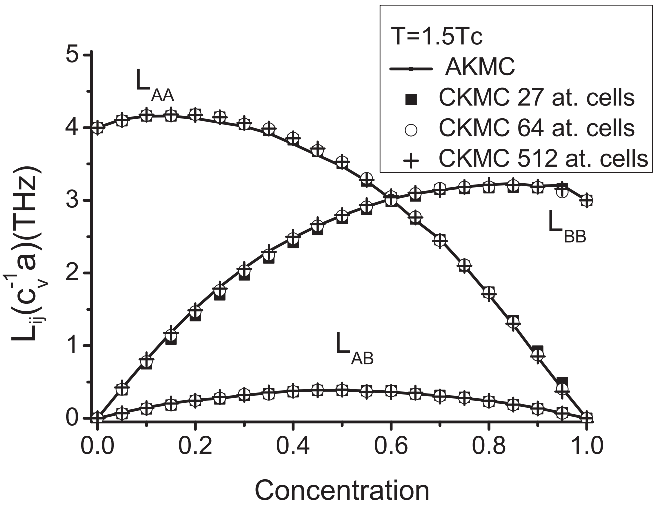

FIG. 10. Normalized Onsager matrix of the first n.n. interaction alloy as a function of the concentration at a temperature $T = 1.5T_c$. The dark line corresponds to AKMC simulations, while the symbols corresponds to CKMC simulations.

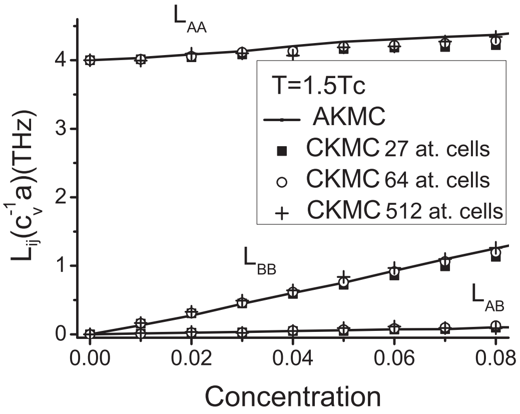

FIG. 11. Normalized Onsager matrix of the first n.n. interaction alloy as a function of the concentration for the model bcc Ising alloy at a temperature $T = 0.8T_c$. The dark line corresponds to AKMC simulations, while the symbols corresponds to CKMC simulations.

a concentration of 2% in Fig. 12 at $T = 1.5T_c$ and in Fig. 13 at $T = 0.8T_c$. The CKMC kinetics performed at different cell sizes perfectly agree with the AKMC reference simulations. These simulations show that the CKMC method is able to produce quantitative simulation of diffusion processes without being impeded by the presence of interactions.

3. CKMC simulation of the Fe-Cu alloy

Finally, a set of interactions describing the Fe-Cu alloy is used to demonstrate the ability of the CKMC method to tackle with the more complex interaction models required to describe real alloys. The Fe-Cu alloy adopts in the Fe-rich domain a bcc structure up to a temperature of 850 °C, above which an allotropic phase transformation takes place. A miscibility gap limits the solubility of copper in the iron matrix to a maximum of 1.8 at.% at 850 °C. The copper precipitates adopt a bcc structure up to a radius of 2 nm, beyond which faulted structure and finally the fcc structure of pure copper is preferred. A parametrization of AKMC simulations for this alloy in the bcc structure has been established from density functional theory calculations by Soisson and Fu in Ref. 9. Using these parameters, detailed in Tables II and III, the thermodynamic properties of the alloys are accurately reproduced below the Curie temperature and to a lesser degree at higher temperatures. The AKMC simulations based on these interactions provide an interesting insight of the kinetic properties of this alloy, showing the high mobility of the copper clusters due to the high vacancy concentration on sites neighboring copper atoms. The ability of the CKMC method to reproduce its phase diagram or interface profile has already been demonstrated in Ref. 27. In the present work, CKMC simulations were performed at $T = 1100$ K in order to benefit from a high solubility, while keeping the bcc structure.

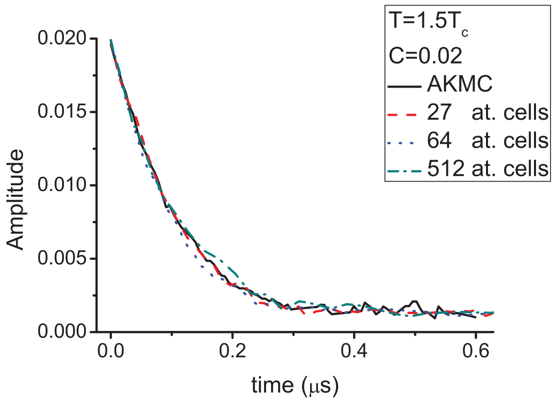

FIG. 12. (Color online) Amplitude of a sinusoidal excitation of wavelength $\lambda = 24a$ as a function of time of a solution of concentration $C = 0.02$ of the first n.n. interaction alloy at $T = 1.5T_c$. The black continuous line corresponds to AKMC simulations, the red dashed (respectively, blue dotted and green dash and dotted) one to 27 (respectively, 64 and 512) at. cells CKMC simulations.

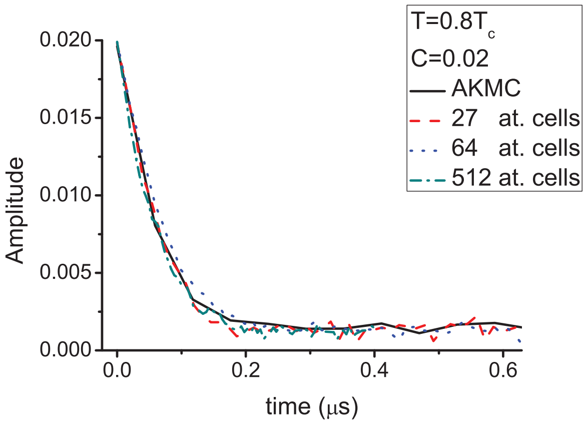

FIG. 13. (Color online) Amplitude of a sinusoidal excitation of wavelength $\lambda = 24a$ as a function of time of a solution of concentration $C = 0.02$ of the first n.n. interaction alloy at $T = 0.8T_c$. The black continuous line corresponds to AKMC simulation, the red dashed (respectively, blue dotted and green dash and dotted) one to 27 (respectively, 64 and 512) at. cells CKMC simulations.

First, the free-energy functional of the Fe-Cu alloy has been computed at 1100 K as shown in Fig. 14. Comparing the AKMC and CKMC results for 4096 atomic site systems, the free energy appears to be overestimated in the miscibility gap by the CKMC calculation. Despite being lower than the energy density of a single 64 atomic site system, the CKMC systems seems to be unable to relax enough to reach the energy density of the AKMC system of identical size. As the free-energy density remains very accurately reproduced in the solid solution, it should not hinder diffusion simulations like the excitation decay, while it will not lead CKMC simulations to produce reliable results concerning precipitate nucleation. As can be seen in the bottom part of Fig. 14, AKMC and CKMC

TABLE II. Binding energies at first and second nearest neighbor distances in the Fe-Cu alloy from Ref. 40.

	first n.n. (eV)	second n.n. (eV)
FeFe	-0.7782	-0.3891
CuCu	-0.6436	-0.3218
FeCu	$-0.6506-7.83\times10^{-6}T$	$-0.3450-3.92\times10^{-6}T$
FeV	-0.191	-0.095
CuV	-0.190	-0.190
VV	-0.000	0.000

TABLE III. Kinetic parameters of the Fe-Cu alloy: binding energies at saddle point position and attempt frequencies, from Ref. 9.

Saddle point interactions	(eV)
FeFe	−1.53
CuCu	−1.41
FeCu	−1.50
CuFe	−1.36
Attempt frequencies	(THz)
Fe	5000
Cu	2000

free-energy densities split at a concentration $c \approx 0.045$ where the AKMC free-energy derivative, the chemical potential, drops, indicating nucleation. This drop does not appear on the CKMC free-energy curve, which seems unable to relax enough for nucleation to happen. This is a sign of the limits of the thermodynamic parametrization procedure used. A solution to this problem might be to introduce in the future a forth order term in the gradient of concentration in the effective Hamiltonian.

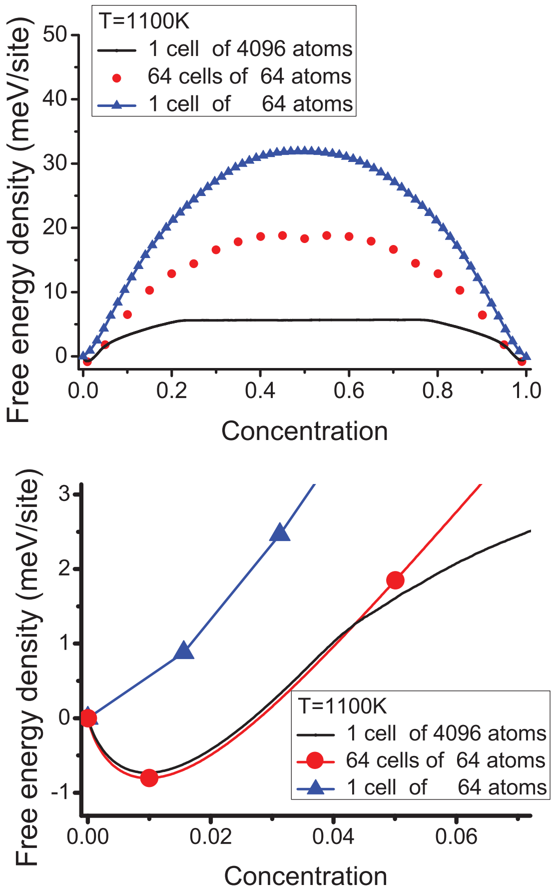

FIG. 14. (Color online) Free-energy density as a function of the concentration for the Fe-Cu alloy at $T = 1100$ K (top), with a focus on the solute solution area (bottom). For the sake of clarity the quantity $F(c) = c \times 0.74$ eV has been deduced from the free energy.

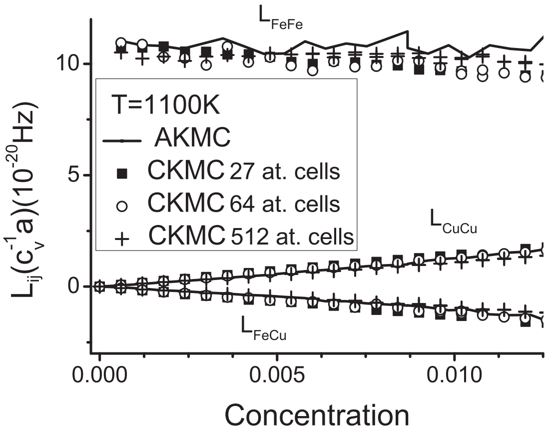

FIG. 15. Normalized Onsager matrix as a function of the concentration for the Fe-Cu alloy at a temperature $T = 1100$ K. The dark line corresponds to AKMC simulations, while the symbols correspond to CKMC simulations at different cell sizes.

The Onsager matrix of the Fe-Cu alloy has been computed in the solid solution using AKMC simulations. As shown in Fig. 15, negative L_{AB} correlations take place. These correlations are however low enough not to induce solute drag by the vacancy. As a consequence, the $\{(AV),(BV),(VAVB)\}$ subset of events is used for simulations at the coarse-grained scale, with the frequencies

$$\begin{aligned}\tilde{W}^0_{AV}(c) &= \frac{S}{dz^*}(L_{AA}+L_{AB}),\\ \tilde{W}^0_{BV}(c) &= \frac{S}{dz^*}(L_{BB}+L_{AB}),\\ \tilde{W}^0_{VAVB}(c) &= \frac{S}{dz^*}\frac{1}{2}(-L_{AB}),\\ \tilde{W}^0_{VBVA}(c) &= \frac{S}{dz^*}\frac{1}{2}(-L_{AB}).\end{aligned}\tag{24}$$

The CKMC frequencies are then parameterized on a linear fit of the AKMC measurements of the Onsager matrix. As can be observed in Fig. 15, an accurate reproduction of the different terms of the Onsager matrix is achieved. The accuracy obtained despite the important kinetic correlations that take place in this system at the atomic scale, indicates that the hypothesis that correlations can be neglected at the cellular scale is robust.

The simulation of the decay of a sinusoidal excitation of amplitude $A = 0.005$ in a solution of concentration $c = 0.005$ in Cu atoms is displayed on Fig. 16. A semiquantitative agreement is obtained between AKMC and CKMC simulations, with a systematic underestimation of the decay time with 27 atomic site cells and an overestimation with the 512 atomic site cells. However, the quantitative disagreement remains below 25% of the AKMC decay time. This discrepancy could also come from the thermodynamic parametrization of the cellular interaction. This interaction affects the driving force out of equilibrium and thus the decay.

C. Reliability and efficiency of CKMC simulations

The limitations and advantages of the CKMC method have been further investigated to define its field of application. The effect of the solute concentration and of the wavelength on the excitation decay simulations is investigated on the bcc alloys with first nearest neighbor interactions presented earlier.

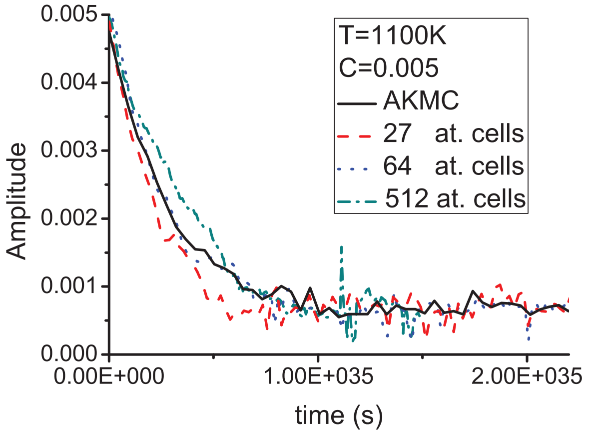

FIG. 16. (Color online) Amplitude of a sinusoidal excitation of wavelength $\lambda = 24a$ as a function of time of a solution of concentration $C = 0.005$ of the Fe Cu alloy. The black continuous line corresponds to AKMC simulation, the red dashed (respectively, blue dotted and green dash and dotted) one to 27 (respectively, 64 and 512) at. cells CKMC simulations. The dark line corresponds to AKMC simulations, while the symbols correspond to CKMC simulations.

The capabilities of CKMC simulations are then exemplified on the kinetics of a precipitate dissolution. The gain of CPU time obtained by using CKMC simulations instead of AKMC simulations is then measured.

1. *Systematic study of excitation decay*

In order to measure the impact of the length scale of the microstructure on the ability of the CKMC simulations to reproduce the evolution of a system, a systematic study of decay profiles both with respect to the average concentration and the wavelength is performed. In Fig. 17, the decay time τ is represented as a function of the concentration at $T = 1.5T_c$. The decay time is obtained by an exponential fit $A = A_0 \exp(-t/\tau)$ of the decay of a sinusoidal excitation of wavelength $\lambda = 24a$. The decay time seems approximately linear between $c = 0$ and 0.5 according to AKMC simulations. CKMC simulations provide results in quantitative agreement with AKMC simulations at all concentration, usually within the fitting error bars. No systematic bias appears with concentration, even if a higher dispersion of the results with respect to the cell size can be observed in concentrated systems.

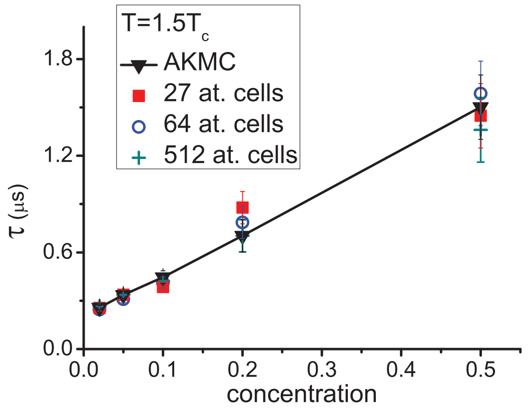

FIG. 17. (Color online) Decay time as a function of the concentration for the first n.n. interactions alloy at a temperature $T = 1.5T_c$. The dark line corresponds to AKMC simulations, while the symbols correspond to CKMC simulations.

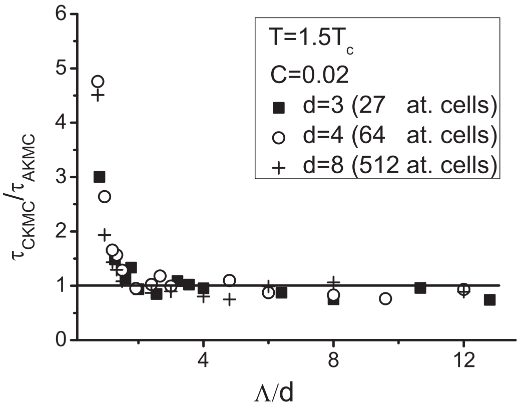

FIG. 18. Ratio between the decay time obtained by CKMC and AKMC simulation as a function of the wavelength in cell size unit at a temperature $T = 1.5T_c$. The dark line is a guide to the eye corresponding to a perfect agreement.

The linear behavior with respect to the concentration is not a general feature of the decay time. In the current case, its occurrence can be interpreted using Figs. 8 and 10. The free energy appears at that temperature to be approximately a parabolic function of the concentration, while the terms of the Onsager matrix can be considered linear for $c \in [0,0.5]$ as a first approximation. These two approximations explain that a decay time linear with respect to the average concentration is found, as detailed in Appendix C.

The impact of the wavelength on the accuracy of CKMC simulations is studied independently. In Fig. 18, the decay time is plotted as a function of the wavelength, in cell size unit. This figure shows that while a good agreement between AKMC and CKMC simulation decay time is found at large wavelength for all cell sizes, with an error bellow 10%, the discrepancy increases suddenly at low wavelength. It is not surprising that phenomena with a length scale close to the resolution are poorly reproduced. Figure 17 allows defining a threshold value of two cell sizes for the wavelength, below which kinetic properties are not correctly reproduced. The use of the (VVAB) exchange for CKMC simulations reduces the kinetic resolution of the simulation, as for this event two consecutive exchanges in a given direction are considered, against one for the others. However, as the correlation term $L_{AB} < L_{BB}, L_{AA}$, the (VVAB) exchanges do not dominate the diffusion and cannot explain the sharp increase of the decay time ratio. A slightly lower kinetic resolution of CKMC simulation can thus be expected for highly correlated systems.

2. *Dissolution of a precipitate*

Simulations of the dissolution of a solute precipitate have been performed on the alloy with first n.n. interactions to demonstrate the ability of the CKMC method to perform simulations of microstructure evolutions. At $T = 1.5T_c$, in a 48^3 atomic site simulation box, simulations of the dissolution

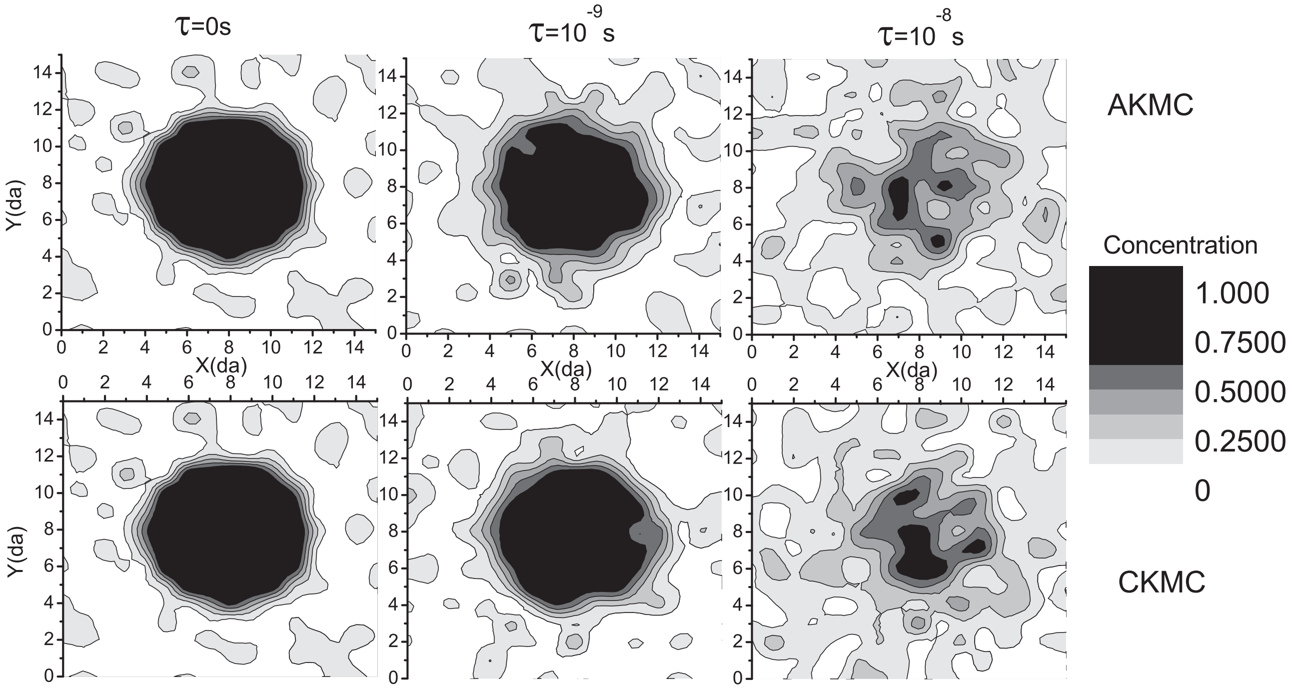

FIG. 19. Contour map of the concentration field along a cross-section during the dissolution of a precipitate simulated by the AKMC method (top) and the CKMC method (bottom) with 27 atomic site cells, with from left to right the field in the initial configuration, and after 10^{-9} and 10^{-8} s. da is the size of the cellular unit cell. For the present contour map, the AKMC concentration field is averaged on cells of 27 atomic sites to mimic the resolution of the CKMC simulation.

of a spherical precipitate of concentration $c = 0.9$ and of radius $R = 12a$ in a matrix of concentration $c = 0.1$ have been performed using both AKMC and CKMC methods. Contour maps representing the concentration field in a two dimensional cross-section of the system are shown in Figs. 19 and 20. The quantitative agreement is assessed using the radial concentration profile from the center of the precipitate $c(r)$. These profiles, represented in Figs. 21 and 22 at two different time scales, allow assessing quantitatively the ability of CKMC simulations to reproduce the evolution of realistic microstructures. When cells are small enough, CKMC simulations can accurately reproduce the concentration field, including the precipitate. This is the case with 27 and 64 atomic site cells, and in such a case the evolution of the profile obtained by CKMC simulations agrees well with the profiles obtained by AKMC simulations. However, when cells are large compared to the precipitate size, as it is the case with 512 atomic site cells, the poor resolution does not allow obtaining an accurate profile within the precipitate. Despite this fact, CKMC simulations quantitatively reproduce the AKMC concentration of cells beyond the third nearest neighbor position from the center of the precipitate and further away. Thus the poor description of the precipitate seems not to impair predictions of the evolution of the matrix, where concentration gradients are smaller. In the present alloy, the solubility of vacancies is higher at the interface between the precipitate and the matrix. The good agreement obtained between AKMC and CKMC simulation concerning the evolution of the shape of the interface with time illustrates the ability of the CKMC simulation to reproduce the increased atomic mobility at the interface due to this vacancy concentration, resulting in an increase of the interdiffusion coefficient at the matrix-precipitate interface. Moreover, these simulations show that good driving forces were obtained despite the large concentration gradient.

3. *Acceleration coefficient*

To evaluate the gain of computational time, an acceleration coefficient $A = \frac{\tau^{\mathrm{CPU}}_{\mathrm{AKMC}}}{\tau^{\mathrm{CPU}}_{\mathrm{CKMC}}}$ corresponding to the ratio of CPU times required by the AKMC and the CKMC method to reach a given physical time is measured at equilibrium. These measurements are displayed in Fig. 23. In the case of the first n.n. interaction alloy, the acceleration coefficient appears to be fairly robust with respect to the concentration or the temperature, with an acceleration coefficient up to a 5 for 512 atomic site cells. A gradient of concentration such as can be observed during excitation decay measurements appeared to affect it by less than 10%. In the case of the Fe-Cu alloy, an impressive acceleration coefficient of nearly 2500 is obtained.

A transition from a configuration to another requires more CPU time in a CKMC simulation than in an AKMC simulation, as the high number of possible values of the concentration field forbid storing all transition frequencies in memory, and because several kinetic events are possible between two cells in a CKMC simulation against only one between two atomic sites in a AKMC simulation. However, each CKMC step is more effective, as correlations are already integrated within an event and as a longer distance is covered in each exchange. The acceleration arising from the integration of the correlations is mostly independent of the cell size, while the acceleration due to the range of the kinetic events is a function of the cell size d. From random walk theory, the number of steps

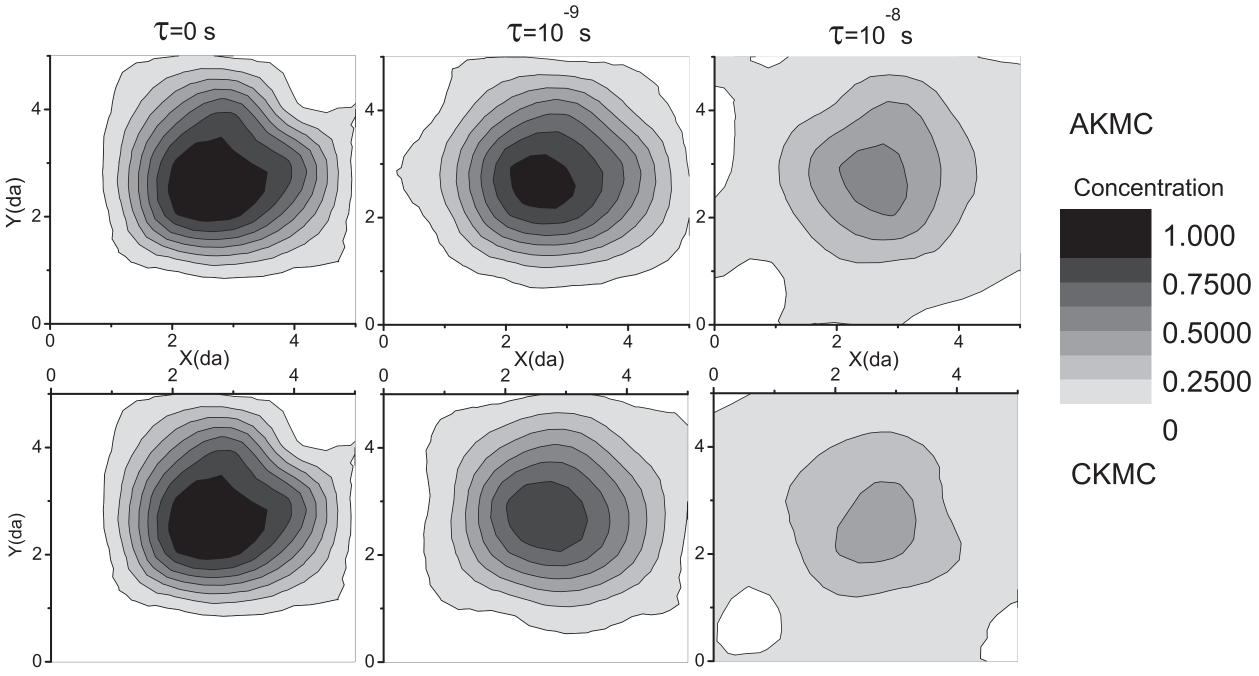

FIG. 20. Contour map of the concentration field along a cross-section during the dissolution of a precipitate simulated by the AKMC method (top) and the CKMC method (bottom) with 512 atomic site cells, with from left to right the field in the initial configuration, and after 10^{-9} and 10^{-8} s. da is the size of the cellular unit cell. For the present contour map, the AKMC concentration field is averaged on cells of 512 atomic sites to mimic the resolution of the CKMC simulation.

to reach any given state should scale with d^{-2} for a diffusive behavior. A power law fit $A = \alpha d^b$ of the CKMC acceleration coefficient gave subdiffusive exponents $b \in [1.6,1.9]$. With only three different cell sizes available, the accuracy of the adjustment is however limited. The acceleration coefficient of the Fe-Cu alloy is found to be of the order of 10^3 higher than the acceleration coefficient of the first n.n. interaction alloy. This can be explained by considering the effect of kinetic correlations: when vacancies are strongly interacting with solute atoms, most steps are used by the vacancy to escape the volume of interaction with the solute. By considering effective exchanges at a larger distance, a single step is required in a CKMC simulation, sparing a lot of computational time. This is typically the case of the Fe-Cu alloy. Several different Monte Carlo algorithms can be used for AKMC simulations as well as CKMC simulations. The residence time algorithm used in all this work is more efficient when there is a large difference between the frequencies of the different kinetic events[30] as it is the case for the AKMC simulation of the Fe-Cu alloy. The gain observed can thus not be noticeably reduced by a better choice of Monte Carlo algorithm.

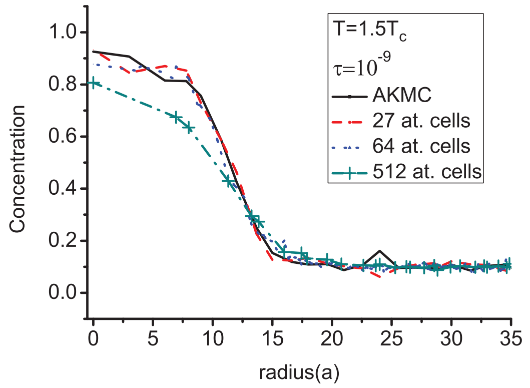

FIG. 21. (Color online) Radial concentration profile during the dissolution of a precipitate after a time $\tau = 10^{-9}$ s. The black continuous line corresponds to AKMC simulation, the red dashed one (respectively, blue dotted and green dash and dotted) to 27 (respectively, 64 and 512) at. cell CKMC simulations. Simulation points for the 512 at. cells are marked by plus symbols.

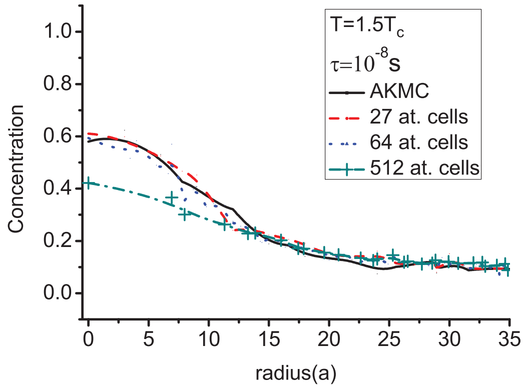

FIG. 22. (Color online) Radial concentration profile during the dissolution of a precipitate after a time $\tau = 10^{-8}$ s. The black continuous line corresponds to AKMC simulation, the red dashed one (respectively, blue dotted and green dash and dotted) to 27 (respectively, 64 and 512) at. cell CKMC simulations.

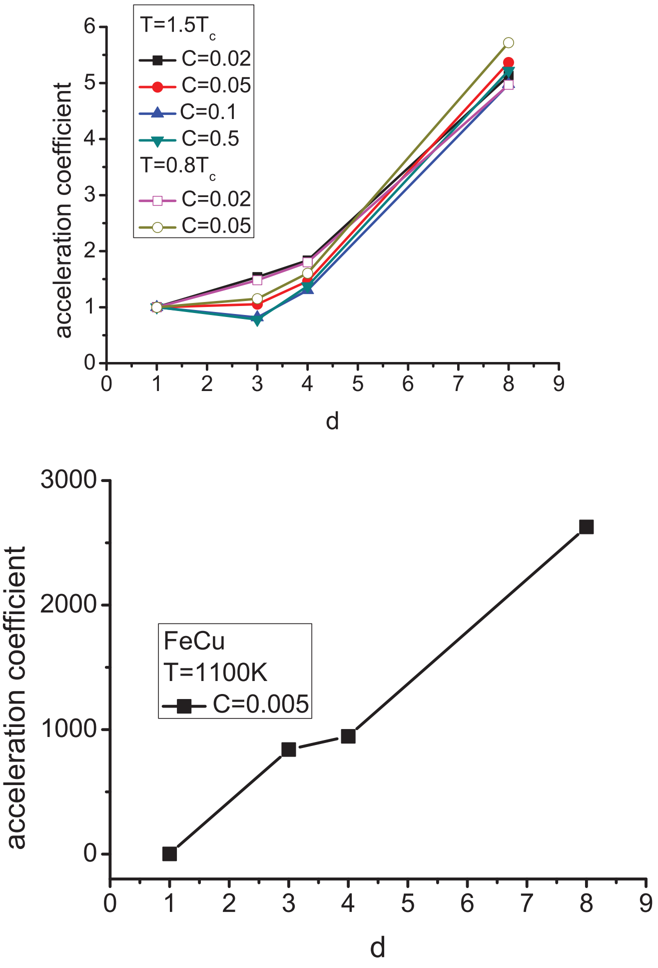

FIG. 23. (Color online) Acceleration coefficient as a function of the cell size d for the first n.n interaction alloy and different solute concentration C (top) and for the Fe-Cu alloy (bottom).

IV. CONCLUSION

To bridge the gap between atomic and macroscopic simulations, a coarse-grained master equation is built from the atomic scale master equation, by using the local equilibrium approximation. The constraints originating from the Onsager matrix are used to define the transition frequencies at the coarse-grained scale. We propose to perform a time integration of the master equation thus obtained by using a Monte Carlo algorithm that keeps the discrete aspect of atoms: the coarse-grained kinetic Monte Carlo method.

The CKMC method is entirely parameterized using atomic scale Monte Carlo simulations in a bottom up approach. The kinetic parametrization introduced allows reproducing complex kinetic phenomena like flux couplings. The Onsager matrices obtained in CKMC simulations at all scales agree with the measurement of the Onsager matrix in AKMC simulations. This agreement confirms the validity of the method in equilibrium situations. The study of the decay of a sinusoidal excitation or the dissolution of a precipitate shows the ability of the method to produce reliable simulations of out of equilibrium systems. Simulations of the dissolution of precipitates shows the ability of the method to provide predictive simulations of microstructures in three dimensions. Moreover, this method is shown to be very efficient on strongly correlated systems like in the case of the Fe-Cu alloy, where a speed up of the order of 10^3 is obtained.

While the present work focuses on the vacancy-mediated diffusion mechanism which is the main mechanism controlling thermal evolution, the interstitial-mediated diffusion mechanism can be described as well by using the corresponding atomic-scale simulation for the parametrization. Most properties and techniques used in AKMC simulations can be similarly transferred to CKMC simulations like the time renormalization techniques serving to restore equilibrium vacancy concentration used in recent AKMC simulations.[41] As a consequence, the CKMC method appears as a ready to use method for diffusion problems, able to provide reliable predictions of the microstructure evolutions for a lower CPU time than the one required by AKMC simulations.

A next step would be to apply the CKMC method to the simulation of phase decomposition. The hypothesis of local equilibrium at the root of this work is likely to cause problems for the simulation of nucleation. An adaptive method, where the mesh size would evolve with the microstructure could be designed for that purpose, as the CKMC method is proved to be consistent with both a fine and a coarse mesh. The beginning of phase decomposition could be treated at the atomic scale. Then, the mesh could be progressively coarsened during the growth and coarsening regimes.

ACKNOWLEDGMENTS

The authors would like to thank Pascal Bellon for the fruitful discussions on the subject, Alphonse Finel and Yann Le Bouar for their deep interest into the development of this method, and Frédéric Soisson for his keen advices on the Fe-Cu system. Part of this work has been funded by the European FP7 Perform project.

APPENDIX A: RESIDENCE TIME ALGORITHM

In a Monte Carlo simulation of diffusion on a rigid lattice, several algorithms can be used, like the Metropolis algorithm[38] or the residence time algorithm.[39] For kinetic simulations, both algorithms present some advantages, that are discussed in details in Ref. 30.

Concerning the residence time algorithm used in the present work, at each iteration the following operations are performed. (1) The list $\{\dot{\mathbf{n}}\}$ of the configurations at reach in a single step from the current configuration is updated. (2) The transition rates $W(\mathbf{n} \to \dot{\mathbf{n}})$ of each transition is computed. (3) A random number R of uniform probability over $[0,1[$ is drawn. (4) The event i for which $\sum_{\mathbf{n}_j \in \{\dot{\mathbf{n}}\}}^{i-1} W(\mathbf{n} \to \mathbf{n}_j) \leqslant R < \sum_{\mathbf{n}_j \in \{\dot{\mathbf{n}}\}}^{i} W(\mathbf{n} \to \mathbf{n}_j)$ is then chosen. (5) The physical time of the simulation is increased by the inverse of the sum of the transition rates $\Delta t = \frac{1}{\sum_{\dot{\mathbf{n}}} W(\mathbf{n} \to \dot{\mathbf{n}})}$. (6) The chosen transition is applied.

APPENDIX B: THERMODYNAMIC AVERAGE OF THE COARSE-GRAINED JUMP FREQUENCIES

The coarse-grained jump frequencies $W^0_{\mathbf{N},\dot{\mathbf{N}}}$ depend formally on the local concentration c, but also on all the other

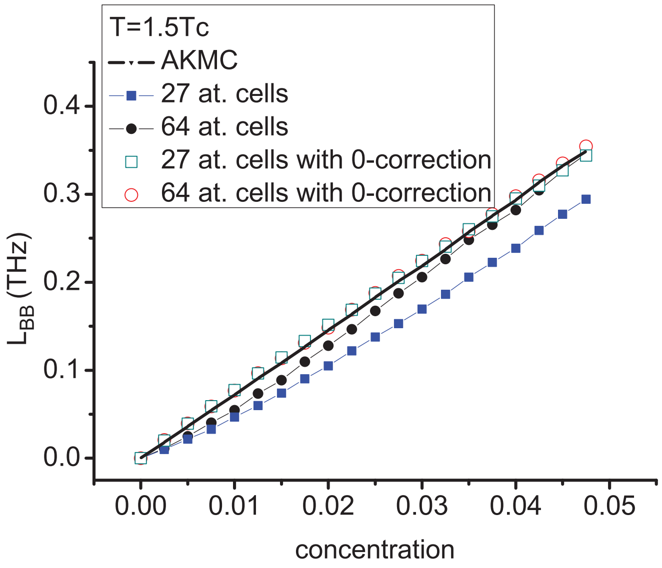

FIG. 24. (Color online) L_{BB} term of the normalized Onsager matrix as a function of the concentration in the dilute limit of a bcc alloy with first n.n interactions. The dark line corresponds to AKMC simulations, while the symbols correspond to CKMC simulations.

degrees of freedom at the coarse-grained scale. In the continuum limit, these configurations follow a Gaussian distribution according to the Boltzmann law and the substitution of the configuration-dependent quantity $W^0_{XY}(\mathbf{N})$ with the average value $\tilde{W}^0_{XY}(c)$ is consistent. The study of nonlinear kinetic effects is beyond the scope of this work. However, for small cells, the continuum limit is not valid and a Gaussian distribution of states cannot always be assumed. In this case, discretization induces kinetic finite size effects.

When an alloy is dilute in solute atoms, as the solute concentration involved in the exchange frequency is the average concentration of two cells, there is a nonvanishing probability that one of the cells has no solute atom and the second one contains $c \times N_{\text{tot}}$ solute atoms. Thus any exchange involving the displacement of a solute atom from the first cell has to be rejected. The effect of these rejections is negligible as long as the Gaussian approximation holds. However, these rejections have a significant impact on the kinetic properties of a dilute alloy. Figure 24 shows the Onsager matrix of the first n.n. interaction alloy, as computed by CKMC simulations, with a focus on the dilute case. It can be seen on that figure that for small cells of $N_{\text{tot}} = 27$ and 64 sites, the mobility of the atoms is underestimated for concentrations $c < c_0 \approx \frac{1}{N_{\text{tot}}}$. At this concentration, a significant number of cells devoid of any solute atoms appears. This corresponds to a case where the assumption that $\nabla c/c \to 0$ does not hold. The probability to obtain a configuration where a given exchange is impossible can, however, be evaluated. For example, in the case of (BV) exchanges, the average $\tilde{W}^0_{BV}(c)$ of the rate of (BV) exchanges to take place in a system of two cells of overall population of B atoms N is

$$\tilde{W}^0_{BV}(N/2N_{\text{tot}}) = \sum_{i=0}^{N} P(i,N-i)W^0_{BV}(i,N-i), \qquad \text{(B1)}$$

where $P(i,N-i)$ is the probability to find a concentration i in the first of these two cells, and $N-i$ in the other. By keeping only the leading term in the gradient of concentration, the exchange probability $W^0_{BV}(i,N-i)$ is independent of i as long as $i > 0$, and null otherwise. The last equation can then be restated:

$$W^0_{BV}(i,N-i) = W^0_{BV}(N) = \frac{\tilde{W}^0_{BV}(N/2N_{\text{tot}})}{[1-P(0,N)]}. \qquad \text{(B2)}$$

The exchanges used in CKMC simulations can therefore be increased to compensate these rejected exchanges. $P(0,N)$ can easily be evaluated using a mean-field approximation. We consider two cells of N_{tot} sites each, sharing a total of N solute atoms and a single vacancy. Assuming that all the configurations defined by the position of the solute atom have a same probability, the probability for a cell to be empty can be evaluated from a simple combinatorial calculation:

$$P(0,N) = \frac{C^N_{N_{\text{tot}}-1}}{C^N_{2N_{\text{tot}}-1}} \xrightarrow[N_{\text{tot}}\gg 1]{} \left(\frac{1}{2}\right)^N. \qquad \text{(B3)}$$

For a B-V exchange the event probability can thus be written as

$$W_{BV}(N) = \frac{\tilde{W}^0_{BV}(N/2N_{\text{tot}})}{1-\left(\frac{1}{2}\right)^N}, \qquad \text{(B4)}$$

while the probability for an A-V event is obtained by substituting $2N_{\text{tot}} - N - 1$ to N:

$$W_{AV}(N) = \frac{\tilde{W}^0_{AV}(N/2N_{\text{tot}})}{1-\left(\frac{1}{2}\right)^{2N_{\text{tot}}-N-1}}. \qquad \text{(B5)}$$

Similar combinatoric calculations lead to corrections to the probabilities of the other events:

$$\begin{aligned}
W_{VAVB}(N) &= \frac{\tilde{W}^0_{VAVB}(N/2N_{\text{tot}})}{\left[1-\left(\frac{1}{2}\right)^{2N_{\text{tot}}-N-1}\right]\left[1-\left(\frac{1}{2}\right)^N\right]},\\
W_{VABB}(N) &= \frac{\tilde{W}^0_{VABB}(N/2N_{\text{tot}})}{\left[1-\left(\frac{1}{2}\right)^N-\frac{N}{2N_{\text{tot}}}\left(\frac{1}{2}\right)^{N-1}\right)\left[1-\left(\frac{1}{2}\right)^{2N_{\text{tot}}-N}\right]},\\
W_{VVAB}(N) &= \frac{\tilde{W}^0_{VVAB}(N/2N_{\text{tot}})}{\left[1-\left(\frac{2}{3}\right)^N\right]\left[1-\left(\frac{2}{3}\right)^{3N_{\text{tot}}-N}\right]}. \qquad \text{(B6)}
\end{aligned}$$

This "0-correction," different for each type of jump, relies on a crude approximation. In Fig. 24, the L_{BB} of an alloy with first n.n. interactions, detailed in Sec. III B2, computed with and without the 0-correction, are represented. The 0-correction leads to an accurate reproduction of the AKMC results by CKMC simulations with cells of various sizes. It can be noticed from these expressions that the 0-correction does not hinder the detailed balance.

APPENDIX C: DIFFUSION EQUATION

The linear behavior of the decay time with respect to the concentration can be understood by considering the diffusion equation:

$$\frac{\partial c_i((x),t)}{\partial t} = \sum_k D_{ik}\nabla^2 c_k(\mathbf{x},t), \qquad \text{(C1)}$$

where the diffusivity matrix D_{ik} can be built from the free energy and the Onsager matrix:

$$D_{ik} = \beta \sum_j L_{ij} \frac{\partial \mu_j}{\partial c_k} = \beta \sum_j L_{ij} \frac{\partial^2 F}{\partial c_k \partial c_j}, \qquad \text{(C2)}$$

where β is the inverse thermodynamic temperature. As a consequence, for a sinusoidal concentration field, a parabolic free energy and a linear Onsager matrix lead to a decay time linear with respect to the average concentration.[42]

---

[*] tgarnier@illinois.edu

[1] V. I. Yelagin, V. V. Zakharov, S. G. Pavlenko, and T. D. Rostova, Phys. Met. Metall. **60**, 88 (1986).

[2] E. Clouet, L. Laé, T. Épicier, W. Lefebvre, M. Nastar, and A. Deschamps, Nat. Mater. **5**, 482 (2006).

[3] F. Danoix, E. Bemont, P. Maugis, and D. Blavette, Adv. Eng. Mat. **8**, 1202 (2006).

[4] Z. Mao, C. K. Sudbrack, K. E. Yoon, G. Martin, and D. N. Seidman, Nat. Mater. **6**, 210 (2007).

[5] T. Garnier, M. Nastar, P. Bellon, and D. R. Trinkle, Phys. Rev. B (2013).

[6] Z. Jiao and G. Was, Acta Mater. **59**, 1220 (2011).

[7] M. Nastar, Phil. Mag. A **85**, 641 (2005).

[8] A. J. Ardell, in *Radiation-Induced Solute Segregation in Alloys in Materials issues for Generation IV Systems*, NATO Science for Peace and Security Series B: Physics and Biophysics (Springer, New York, 2008), pp. 285–310.

[9] F. Soisson and C. C. Fu, Phys. Rev. B **76**, 214102 (2007).

[10] T. Jourdan, F. Soisson, E. Clouet, and A. Barbu, Acta Mater. **58**, 3400 (2010).

[11] T. Jourdan, J.-L. Bocquet, and F. Soisson, Acta Mater. **58**, 3295 (2010).

[12] M. Nastar and F. Soisson, in *Comprehensive Nuclear Materials* (Elsevier, Amsterdam, 2012), pp. 471–497.

[13] L. Q. Hu and S. Y. Chen, Acta Mater. **49**, 1879 (2001).

[14] P. Bellon, in *Comprehensive Nuclear Materials* (Elsevier, Amsterdam, 2012), pp. 411–432.

[15] S. Hu and C. H. J. Henager, J. Nucl. Mater. **394**, 155 (2009).

[16] S. Hu and C. J. Henager, Acta Mater. **58**, 3230 (2010).

[17] H. Wan, Y. Shen, X. Jin, Y. Chen, and J. Sun, Acta Mater. **60**, 2528 (2012).

[18] V. Vaithyanathan, C. Wolverton, and L. Q. Chen, Phys. Rev. Lett. **88**, 125503 (2002).

[19] M. A. Katsoulakis, A. J. Majda, and D. G. Vlachos, Proc. Natl. Acad. Sci. USA **100**, 782 (2003).

[20] M. Katsoulakis and D. Vlachos, J. Chem. Phys. **119**, 9412 (2003).

[21] A. Chatterjee, M. A. Katsoulakis, and D. G. Vlachos, Phys. Rev. E **71**, 026702 (2005).

[22] A. Chatterjee and D. Vlachos, J. Chem. Phys. **124**, 064110 (2006).

[23] P. Castrillo, R. Pinacho, M. Jaraiz, and J. E. Rubio, J. Appl. Phys. **109**, 103502 (2011).

[24] K. Kaski, K. Binder, and J. D. Gunton, Phys. Rev. B **29**, 3996 (1984).

[25] J. S. Langer, M. Bar-on, and H. D. Miller, Phys. Rev. A **11**, 1417 (1975).

[26] Q. Bronchart, Y. Le Bouar, and A. Finel, Phys. Rev. Lett. **100**, 015702 (2008).

[27] T. Garnier, A. Finel, Y. Le Bouar, and M. Nastar, Phys. Rev. B **86**, 054103 (2012).

[28] H. Eyring, J. Chem. Phys. **3**, 107 (1935).

[29] G. Vineyard, J. Phys. Chem. Solids **3**, 121 (1957).

[30] A. Chatterjee and D. G. Vlachos, J. Comput,-Aided Mater. Des. **14**, 253 (2007).

[31] Q. Bronchart, Ph.D. thesis, Université Cregy-Pointoise, 2006.

[32] The sign of the product $n_\gamma^\sigma n_\gamma^\alpha$ is the same for an exchange $n \rightarrow m$ or an exchange $m \rightarrow n$. This ensures that $L_{\alpha\sigma}$ do not depend on the direction of the exchange.

[33] N. Pottier, *Physique Statistique hors D'équilibre:Processus Irréversibles Linéaires* (EDP-Sciences, Paris, France, 2007).

[34] I. Belova and G. E. Murch, Phil. Mag. **83**, 377 (2003).

[35] I. Belova and G. E. Murch, Phil. Mag. **83**, 393 (2003).

[36] A. R. Allnatt and A. B. Lidiard, *Atomic Transport in Solids* (Cambridge University Press, Cambridge, 1993).

[37] T. Garnier, V. R. Manga, D. R. Trinkle, M. Nastar, and P. Bellon, Phys. Rev. B **88**, 134108 (2013).

[38] N. Metropolis, A. Rosenbluth, M. Rosenbluth, A. Teller, and E. J. Teller, J. Chem. Phys. **21**, 1087 (1953).

[39] W. Young and E. Elcock, Proc. Phys. Soc. **89**, 735 (1966).

[40] F. Soisson and C.-C. Fu, Solid State Phenomena **139**, 107 (2008).

[41] M. Nastar and F. Soisson, Phys. Rev. B **86**, 220102 (2012).

[42] A. L. Greer and F. Spaepen, in *Synthetic Modulated Structures*, edited by L. L. Chang and B. C. Giessen (Academic Press, Orlando, FA, 1985).